J|A|C|S ARTICLES

Published on Web 08/12/2009

Self-Assembly from the Gas-Phase: Design and Implementation of Small-Molecule Chromophore Precursors with Large Nonlinear Optical Responses

David Frattarelli,[†] Michele Schiavo,[‡] Antonio Facchetti,[‡] Mark A. Ratner,*[,†] and Tobin J. Marks*[,†]

Department of Chemistry and the Materials Research Center, Northwestern University, 2145 Sheridan Road, Evanston, Illinois 60208-3113

Received January 19, 2009; E-mail: t-marks@northwestern.edu; ratner@chem.northwestern.edu

Abstract: Efficiently organizing molecular nonlinear optical (NLO) chromophores having large first-order hyperpolarizabilities (β) into acentric microstructures for electro-optic (EO) applications represents a significant materials synthesis and processing challenge, in part due to interchromophore dipolar interactions that promote centrosymmetric organization. Here we report the computational modeling, synthesis, and characterization of a series of eight heteroaromatic organic chromophores, designed to self-organize from the vapor phase via directed hydrogen-bond networks, into acentric thin films. Introduction of α,ω-donor−acceptor hydrogen-bonding substituents along the molecular long axes tunes properties such as hyperpolarizability, volatility, thermal stability, film-forming properties, and macroscopic NLO response ($\chi^{(2)}$). DFT-level molecular modeling, INDO/S optical property analysis, and sum-overstates computation indicate that molecular-core fluorination and hydrogen-bond donor incorporation can increase β_{vec} up to 40× versus that of typical fluorine-free chromophores. Furthermore, inclusion of sterically induced biphenyl conjugative decoupling between chromophore π-donor substituents and the hydrogen-bonding donor sites increases β by ∼50%. Experimental thin-film second harmonic generation (SHG) spectroscopy confirms these trends in calculated responses, with $\chi^{(2)}$ increasing 7.5× upon chromophore core fluorination and 15× with hydrogen-bonding donor substitution, thereby achieving macroscopic responses as high as 302 pm/V at $\omega_o = 1064$ nm. In addition to response trends, cluster calculations also reveal linear additivity in β_{vec} with catenation for all benzoic acid-containing chromophores up to longitudinally aligned trimers. Linear scaling of SHG response with film thickness is observed for benzoic acid-containing chromophores up to 1.0 μm film thickness.

Introduction

There is great current fundamental scientific and technology-driven interest in realizing "all-organic" opto-electronics, specifically those employing high-performance organic electro-optic materials as active components.[1−3] Properties such as molecularly tunable response, very large electro-optic (EO) coefficients (r_{33}s), lower cost, facile synthesis, and lower dielectric constants make organics viable alternatives to single-crystal inorganic $LiNbO_3$ and potassium dihydrogen phosphate (KDP).[4] The larger responses of these molecule-based materials should afford greater data transmission rates, enhanced optical network speed, capacity, and bandwidth in the terabit regime for both data networking and telecommunications.[1−3] Molecule-based organic EO materials must have large first-order hyperpolarizabilities (β), bulk microstructural acentricity as their inorganic counterparts, thermal-/photostability, and temporal stability of the noncentrosymmetric order, for efficient device function.[1−3] Thus, the challenges in molecular EO materials not only involve developing novel constituent chromophore molecules with large intrinsic response properties but also in devising strategies to organize them in acentric microstructures. There are now several chromophore families known that have very large hyperpolarizabilities. However, major factors such as interchromophore electrostatic (dipolar) interactions, guest−host incompatibility, and chromophore shape have impacted electro-optic activity enhancement.[2,3,5] As a result, efficient methodologies for the self-organizing polar chromophores remain a crucial challenge. Currently, there are several strategies for achieving various degrees of noncentrosymmetric thin-film molecular order: (1) glassy polymer/sol−gel electric-field poling,[1−3,5] (2) Langmuir−Blodgett film transfer,[6] (3) layer-by-layer covalent self-assembly (SAS),[7−10] and vapor-phase self-assembly by physical vapor

[†] Department of Chemistry.
[‡] Materials Research Center.

(1) For reviews of organic electro-optics, see: (a) Dalton, L. R. In *Handbook of Conducting Polymers*; Skotheim, T. A., Reynolds, J. R., Eds.; CRC Press LLC: Boca Raton, FL, 2007; Chapter 2. (b) *Characterization Techniques and Tabulations for Organic Nonlinear Optical Materials*; Kuzyk, M. G., Dirk, C. W., Eds.; Marcel Dekker: New York, 1998. (c) *Nonlinear Optics of Organic Molecules and Polymers*; Nalwa, H. S., Miyata, S., Eds.; CRC Press: Boca Raton, FL, 1997. (d) *Organic Nonlinear Optical Materials*; Bösshard, Ch., Sutter, K., Prêtre, Ph., Hulliger, J., Flörsheimer, M., Kaatz, P., Günter, P., Eds.; Advances in Nonlinear Optics, Vol. 1; Gordon & Breach: Amsterdam, 1995. (e) *Molecular Nonlinear Optics: Materials, Physics, Devices*; Zyss, J., Ed.; Academic Press: Boston, 1994. (f) *Introduction to Nonlinear Optical Effects in Molecules and Polymers*; Prasad, P. N., Williams, D. J., Eds.; John Wiley: New York, 1991. (g) *Materials for Nonlinear Optics: Chemical Perspectives*; Marder, S. R., Stucky, G. D., Sohn, J. E., Eds.; ACS Symposium Series, Vol. 455; American Chemical Society: Washington, DC, 1991.

10.1021/ja900131y CCC: $40.75

deposition (PVD).[11] Of these methods, the latter two offer the attraction of directional atom−atom bonding to lock in the acentricity,[7−11] hence, organizational stability, mechanical robustness, environmental stability, and nanoscale control of film growth.

Small-molecule PVD processes are widely used in the growth of organic thin films for organic light-emitting diodes (OLEDS) and field-effect transistors (OFETSs) where they provide precise control of film growth rate, film thickness, and film crystallinity.[12] In applying PVD methods to NLO thin-film growth, we envisioned the need for highly directional intermolecular interactions that would promote acentric supramolecular self-assembly as in Scheme 1. The intermolecular interactions in this strategy must have directional predictability, be sufficiently strong to enforce an acentric nanostructure, yet must be sufficiently weak to afford precursor volatility and potential film annealability. Of the possible conceivable bonding motifs, hydrogen-bonded structures offer well-characterized and predictable bonding patterns and strengths that are tunable via the participating donor and acceptor groups.[11a,b,e,13,14]

PVD of molecular chromophores bearing hydrogen-bonding motifs has only occasionally been used for fabricating EO-active

(2) (a) Kang, H.; Facchetti, A.; Jiang, H.; Cariati, E.; Righetto, S.; Ugo, R.; Zuccaccia, C.; Macchioni, A.; Stern, C. L.; Liu, Z.; Ho, S.-T.; Brown, E. C.; Ratner, M. A.; Marks, T. J. *J. Am. Chem. Soc.* **2007**, *129*, 3267. (b) Kim, T.-D.; Kang, J.-W.; Luo, J.; Jang, S.-H.; Ka, J.-W.; Tucker, N.; Benedict, J. B.; Dalton, L. R.; Gray, T.; Overney, R. M.; Park, D. H.; Herman, W. N.; Jen, A. K.-Y. *J. Am. Chem. Soc.* **2007**, *129*, 488. (c) Dalton, L. R.; Sullivan, P. A.; Bale, D. H.; Olbricht, B. C. *Solid-State Elec.* **2007**, *51*, 1263. (d) Rommel, H. L.; Robinson, B. H. *J. Phys. Chem. C* **2007**, *111*, 18765. (e) DeRose, C. T.; Enami, Y.; Loychik, C.; Norwood, R. A.; Mathine, D.; Fallahi, M.; Peyghambarian, N.; Luo, J. D.; Jen, A. K.-Y.; Kathaperumal, M.; Yamamoto, M. *Appl. Phys. Lett.* **2006**, *89*, 131102. (f) Marder, S. R. *Chem. Commun.* **2006**, 131. (g) Locatelli, D.; Quici, S.; Roberto, D.; De Angelis, F. *Chem. Commun.* **2005**, 5405. (h) Baehr-Jones, T.; Hochberg, M.; Wang, G.; Lawson, R.; Liao, Y.; Sullivan, P. A.; Dalton, L.; Jen, A. K. Y.; Scherer, A. *Opt. Express* **2005**, *13* (14), 5216. (i) Sinyukov, A. M.; Leahy, M. R.; Hayden, L. M.; Haller, M.; Luo, J.; Jen, A. K. Y.; Dalton, L. R. *Appl. Phys. Lett.* **2004**, *85* (24), 5827. (j) Dalton, L. R. *Pure Appl. Chem.* **2004**, *76*, 1421. (k) Kajzar, F.; Lee, K.-S. A.; Jen, K.-Y. *Adv. Polym. Sci.* **2003**, *161*, 1. (l) Abbotto, A.; Feverina, L.; Bozio, R.; Facchetti, A.; Ferrante, C.; Pagani, G. A.; Pedron, D.; Signorini, R. *Chem. Commun.* **2003**, 2144. (m) Dalton, L. *Adv. Polym. Sci.* **2002**, *158*, 1. (n) Dalton, L. R.; Steier, W. H.; Robinson, B. H.; Zhang, C.; Ren, A.; Garner, S.; Chen, A.; Londergan, T.; Irwin, L.; Carlson, B.; Fifield, L.; Phelan, G.; Kincaid, C.; Amend, J.; Jen, A. *J. Mater. Chem.* **1999**, *9*, 1905. (o) Molecular Nonlinear Optics: Materials, Phenomena and Devices. Zyss, J., Ed. *Chem. Phys.* **1999**, *245* (Special issue). (p) Verbiest, T.; Houbrechts, S.; Kauranen, M.; Clays, K.; Persoons, A. *J. Mater. Chem.* **1997**, *7*, 2175. (q) Marks, T. J.; Ratner, M. A. *Angew. Chem., Int. Ed. Engl.* **1995**, *34*, 155. (r) Kanis, D. R.; Ranter, M. A.; Marks, T. J. *Chem. Rev.* **1994**, *94*, 195.

(3) (a) Kim, T.-D.; Luo, J.; Cheng, Y.-J.; Shi, Z.; Hau, S.; Jang, S.-H.; Zhou, X.-H.; Tian, Y.; Polishak, B.; Huang, S.; Ma, H.; Dalton, L. R.; Jen, A. K.-Y. *J. Phys. Chem. C* **2008**, *112*, 4355. (b) Gan, H.; Zhang, H.; DeRose, C. T.; Norwood, R. A.; Luo, J.; Liu, B.; Fallahi, M.; Jen, A. K.-Y.; Ho, S.-T.; Peyghambarian, N. *SPIE Proc.* **2007**, *6470*, 64700F. (c) Song, R.; Yick, A.; Steier, W. H. *Appl. Phys. Lett.* **2007**, *90*, 191103. (d) Michalak, R. J.; Kuo, Y.-H.; Nash, F. D.; Szep, A.; Caffey, J. R.; Payson, P. M.; Haas, F.; Mckeon, B. F.; Cook, P. R.; Brost, G. A.; Luo, J.; Jen, A. K.-Y.; Dalton, L. R.; Steier, W. H. *IEEE Photonics Technol. Lett.* **2006**, *18*, 1207. (e) Dalton, L. R.; Jen, A. K.-Y.; Sullivan, P.; Eichinger, B.; Robinson, B. H. *Quantum Opt.* **2006**, *35*, 1. (f) Khan, R. U. A.; Kwon, O.-P.; Tapponnier, A.; Rashid, A. N.; Günter, P. *Adv. Funct. Mater.* **2006**, *16*, 180. (g) Xu, G.; Liu, Z.; Liu, B.; Ho, S.-T.; Zhu, P.; Wang, L.; Yang, Y.; Marks, T. J.; Luo, J.; Tucker, N.; Jen, A. K.-Y. *SPIE Proc.* **2005**, *5935*, 59350Y–1. (h) Dalton, L. R.; Jen, A. K.-Y.; Steier, W. H.; Robinson, B. H.; Jang, S.-H.; Clot, O.; Song, H. C.; Kuo, Y.-H.; Zhang, C.; Rabiei, P.; Ahn, S.-W.; Oh, M. C. *SPIE Proc.* **2004**, *5351*, 1. (i) Dalton, L. R. *Pure Appl. Chem.* **2004**, *76*, 1421. (j) Lee, M.; Katz, H. E.; Erben, C.; Gill, D. M.; Gopalan, P.; Heber, J. D.; McGee, D. J. *Science* **2002**, *298*, 1401. (k) Ma, H.; Jen, A. K.-Y.; Dalton, L. R. *Adv. Mater.* **2002**, *14*, 1339. (l) Shi, Y.; Zhang, C.; Zhang, H.; Bechtel, J. H.; Dalton, L. R.; Robinson, B. H.; Steier, W. H. *Science* **2000**, *28*, 119.

(4) (a) Sakamoto, T.; Kawanishi, T.; Tsuchiya, M. *Opt. Lett.* **2008**, *33*, 908. (b) Schmidt, W. G.; Albrecht, M.; Wippermann, S.; Blankenburg, S.; Raul, E.; Fuchs, F.; Rodl, C.; Furthmuller, J.; Hermanna, A. *Phys. Rev. C: Nucl. Phys.* **2008**, *77*, 035106. (c) Lucchi, F.; Janner, D.; Belmonte, M.; Balsamo, S.; Villa, M.; Giurgiola, S.; Vergani, P.; Pruneri, V. *Opt. Express* **2007**, *15*, 10739. (d) Binh, L. N. *J. Cryst. Growth* **2006**, *288*, 180. (e) Lin, Z.; Wang, Z.; Chen, C.; Lee, M.-H. *J. Chem. Phys.* **2003**, *118*, 2349. (f) Papuchonn, M.; Combemale, X.; Mathieu, D. B.; Ostrowdky, L.; Reiber, A.; Roy, M.; Sejourne, B.; Werner, M. *Appl. Phys. Lett.* **1975**, *27*, 289.

(5) (a) van der Boom, M. E. *Angew. Chem., Int. Ed.* **2002**, *41*, 3363. (b) Ma, H.; Chen, B.; Sassa, T.; Dalton, L. R.; Jen, A. K.-Y. *J. Am. Chem. Soc.* **2001**, *123*, 986. (c) Hayden, L. M.; Kim, W.-K.; Chafin, A. P.; Lindsay, G. A. *Macromolecules* **2001**, *34*, 1493. (d) Jiang, H.; Kakkar, A. K. *J. Am. Chem. Soc.* **1999**, *121*, 3657. (e) Yitzchaik, S.; Di Bella, S.; Lundquist, P. M.; Wong, G. K.; Marks, T. J. *J. Am. Chem. Soc.* **1997**, *119*, 2995. (f) Ye, C.; Minami, N.; Marks, T. J.; Yang, J.; Wong, G. K. *Macromolecules* **1988**, *21*, 2899. (g) Ye, C.; Marks, T. J.; Yang, J.; Wong, G. K. *Macromolecules* **1987**, *20*, 2322.

(6) (a) Schwartz, H.; Mazor, R.; Khodorkovsky, V.; Shapiro, L.; Klug, J. T.; Kovalev, E.; Meshulam, G.; Berkovic, G.; Kotler, Z.; Efrima, S. *J. Phys. Chem. B* **2001**, *105*, 5914. (b) Ricceri, R.; Neto, C.; Abbotto, A.; Facchetti, A.; Pagani, G. A. *Langmuir* **1999**, *15*, 2149. (c) Roberts, M. J.; Lindsay, G. A.; Herman, W. N.; Wynne, K. J. *J. Am. Chem. Soc.* **1998**, *120*, 11202. (d) Wijekoon, W. M. K. P.; Wijayu, S. K.; Bhawalkar, J. D.; Prasad, P. N.; Penner, T. L.; Armstrong, N. J.; Ezenyilimba, M. C.; Williams, D. J. *J. Am. Chem. Soc.* **1996**, *118*, 4480. (e) Ashwell, G. J.; Jackson, P. D.; Crossland, W. A. *Nature* **1994**, *368*, 438.

(7) (a) Bakiamoh, S. B.; Blanchard, G. J. *Langmuir* **2001**, *17*, 3438. (b) Neff, G. A.; Helfrich, M. R.; Clifton, M. C.; Page, C. J. *Chem. Mater.* **2000**, *12*, 2363. (c) Flory, W. C.; Mehrens, S. M.; Blanchard, G. J. *J. Am. Chem. Soc.* **2000**, *122*, 7976. (d) Roberts, M. J.; Lindsay, G. A.; Herman, W. N.; Wynne, K. J. *J. Am. Chem. Soc.* **1998**, *120*, 11202. (e) Hanken, D. G.; Naujok, R. R.; Gray, J. M.; Corn, R. M. *Anal. Chem.* **1997**, *69*, 240. (f) Katz, H. E.; Wilson, W. L.; Scheller, G. *J. Am. Chem. Soc.* **1994**, *116*, 6636.

(8) (a) Van Cott, K. E.; Guzy, M.; Neyman, P.; Brands, C.; Heflin, J. R.; Gibson, H. W.; Davis, R. M. *Angew. Chem., Int. Ed.* **2002**, *17*, 3226. (b) Facchetti, A.; van der Boom, M. E.; Abbotto, A.; Beverina, L.; Marks, T. J.; Pagani, G. A. *Langmuir* **2001**, *17*, 5939. (c) Huang, W.; Helvenston, M.; Casson, J. L.; Wang, R.; Bardeau, J.-F.; Lee, Y.; Johal, M. S.; Swanson, B. I.; Robinson, J. M.; Li, D.-Q. *Langmuir* **1999**, *15*, 6510. (d) Li, D.-Q.; Swanson, B. I.; Robinson, J. M.; Hoffbauer, M. A. *J. Am. Chem. Soc.* **1993**, *115*, 6975.

(9) (a) Zhu, P.; Kang, H.; van der Boom, M. E.; Liu, Z.; Xu, G.; Ma, J.; Zhou, D.; Ho, S.-T.; Marks, T. J. *SPIE Sympos. Proc.* **2004**, *5621*, 105. (b) van der Boom, M. E.; Evmenenko, G.; Yu, C.; Dutta, P.; Marks, T. J. *Langmuir* **2003**, *19*, 10531. (c) Zhu, P.; van der Boom, M. E.; Kang, H.; Evmenenko, G.; Dutta, P.; Marks, T. J. *Chem. Mater.* **2002**, *14*, 4982. (d) van der Boom, M. E.; Evmenenko, G.; Dutta, P.; Marks, T. J. *Langmuir* **2002**, *18*, 3704. (e) van der Boom, M. E.; Richter, A. G.; Malinsky, J. E.; Dutta, P.; Marks, T. J. *Chem. Mater.* **2001**, *13*, 15.

(10) (a) Facchetti, A.; Abbotto, A.; Beverina, L.; van der Boom, M. E.; Dutta, P.; Evmenenko, G.; Pagani, G. A.; Marks, T. J. *Chem. Mater.* **2003**, *15*, 1064. (b) Facchetti, A.; Abbotto, A.; Beverina, L.; van der Boom, M. E.; Dutta, P.; Evmenenko, G.; Pagani, G. A.; Marks, T. J. *Chem. Mater.* **2002**, *14*, 4996. (c) Lin, W.; Lee, T.-L.; Lyman, P. F.; Lee, J.; Bedzyk, M. J.; Marks, T. J. *J. Am. Chem. Soc.* **1997**, *119*, 2205. (d) Lin, W.; Lin, W.; Wong, G. K.; Marks, T. J. *J. Am. Chem. Soc.* **1996**, *118*, 8034. (e) Yitzchaik, S.; Marks, T. J. *Acc. Chem. Res.* **1996**, *29*, 197. (f) Lin, W.; Yitzchaik, S.; Lin, W.; Malik, A.; Durbin, M. K.; Richter, A. G.; Wong, G. K.; Dutta, P.; Marks, T. J. *Angew. Chem., Int. Ed. Engl.* **1995**, *34*, 1497. (g) Li, D.-Q.; Ratner, M. A.; Marks, T. J. *J. Am. Chem. Soc.* **1990**, *112*, 7389.

(11) (a) Facchetti, A.; Annoni, E.; Beverina, L.; Morone, M.; Zhu, P.; Marks, T. J.; Pagani, G. A. *Nat. Mater.* **2004**, *3*, 910. (b) Zhu, P.; Kang, H.; Facchetti, A.; Evmenenko, G.; Dutta, P.; Marks, T. J. *J. Am. Chem. Soc.* **2003**, *125*, 11496. (c) Rashid, A. N.; Erny, C.; Günter, P. *Adv. Mater.* **2003**, *15*, 2024–2027. (d) Zhu, P.; Kang, H.; Facchetti, A.; Evmenenko, G.; Dutta, P.; Marks, T. J. *J. Am. Chem. Soc.* **2003**, *125*, 11496–11497. (e) Barth, J. V.; Weckesser, J.; Trimarchi, G.; Vladimirova, M.; Vita, A. D.; Cai, C.; Brune, H.; Günter, P.; Kern, K. *J. Am. Chem. Soc.* **2002**, *124*, 7991–8000. (f) Cai, C.; et al. *J. Am. Chem. Soc.* **1998**, *120*, 8563–8564.

Scheme 1. Schematic of the Chromophore PVD Growth Process and Hydrogen-Bonding Directed Acentric Supramolecular Self-Assembly

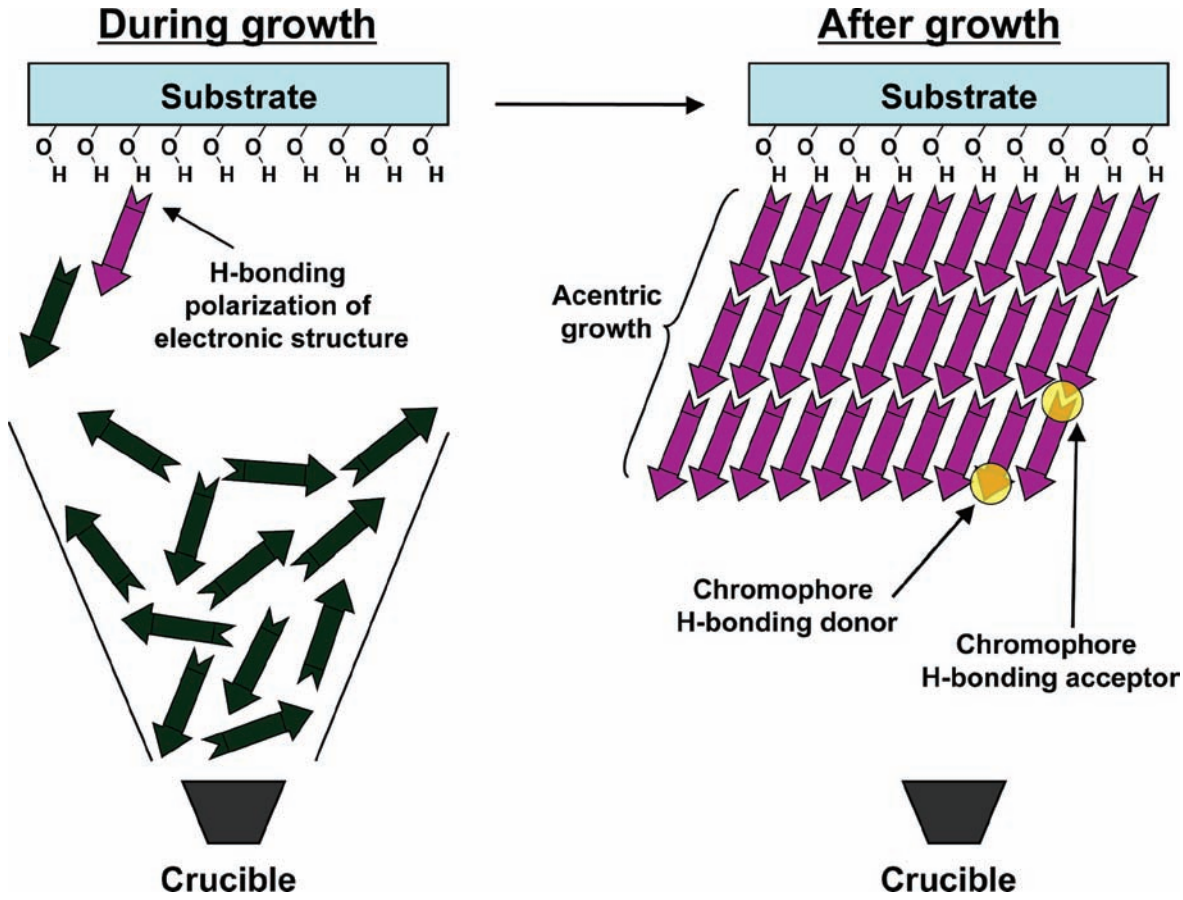

films.[11] In this growth process, combining α,ω-longitudinally functionalized chromophores with hydrogen-bonding donor and acceptor capacities is envisioned to promote polar self-assembly (Scheme 1). To date, the largest second-order susceptibilities ($\chi^{(2)}_{zzz}$) have been up to 95% less than those achieved via self-assembled superlattices and poled-polymers.[5,10,11] To further enhance NLO response, an attractive chromophore design strategy is to select donor-π-acceptor (D-π-A) architectures possessing hydrogen-bonding donor−acceptor functionalities to promote polar self-assembly without compromising volatility and bulk NLO response. Note that unlike typical chromophores used in poling and self-assembly, the β response here can have two sources. In addition to response derived from conjugation length and electron donor−acceptor strength,[1−3] chromophores connected by hydrogen-bonds may experience an additional, hydrogen-bonding-dependent response effects which may either accentuate or depress the bulk NLO response ($\chi^{(2)}$). To account for both types of response and stabilization, while optimizing a parent chromophore such as **1a** (Scheme 2), emphasis was placed in the present study on introducing fluorine (chromophores **2d**, **2e**, **2g**, and **2h**) and conjugative decoupling (chromophores **2c**, **2e**, **2g**, and **2h**) for intrinsic response while simultaneously modifying hydrogen donor−acceptor combinations (**2a**−**2h**) (Scheme 2) for extrinsic bulk response and organization. Regarding molecular fluorination, fluorine substitution should enhance volatility, while for NLO chromophores

(12) (a) DiBenedetto, S. A.; Frattarelli, D.; Ratner, M. A.; Facchetti, A.; Marks, T. J. *J. Am. Chem. Soc.* **2008**, *130*, 7528. (b) Jones, B. A.; Facchetti, A.; Wasielewski, M. R.; Marks, T. J. *J. Am. Chem. Soc.* **2007**, *129*, 15259. (c) Lee, Y. H.; Kim, W. J.; Kim, T. Y.; Yang, J. H.; Cho, K. S.; Hong, J. W.; Shin, J. Y.; Kim, T. W. *Mol. Cryst. Liq. Cryst. Sci. Technol.* **2007**, *462*, 143. (d) Facchetti, A.; Yoon, M.-H.; Stern, C. L.; Hutchison, G. R.; Ratner, M. A.; Marks, T. J. *J. Am. Chem. Soc.* **2004**, *126*, 13480. (e) Cui, J.; Huang, Q.; Veinot, J. C. G.; Yan, H.; Wang, Q.; Fraxedas, J. *Adv. Mater.* **2002**, *14*, 1603. (f) Hutchison, G. R.; Richter, A. G.; Evemenenko, G.; Dutta, P.; Marks, T. J. *Langmuir* **2002**, *18*, 9958. (g) Baldo, M. A.; Kozlov, V. G.; Burrows, P. E.; Forrest, S. R.; Ban, V. S.; Koene, B.; Thompson, M. E. *Appl. Phys. Lett.* **1997**, *71*, 3033.

(13) For hydrogen-bonding reviews, see: (a) Kharlampieva, E.; Sukhishvili, S. A. *J. Macromol. Sci., Polym. Rev.* **2006**, *46*, 377. (b) Hirschberg, J. H. K. Ky.; Koevoets, R. A.; Sijbesma, R. P.; Meijer, E. W. *Chem.—Eur. J.* **2003**, *9*, 4222. (c) Steiner, T. *Angew. Chem., Int. Ed.* **2002**, *41*, 48. (d) Karpfen, A. *Adv. Chem. Phys.* **2002**, *123*, 469. (e) Prins, L. J.; Reinhoudt, D. N.; Timmerman, P. *Angew. Chem., Int. Ed.* **2001**, *40*, 2382. (f) *Structure & Bonding*; Fujita, M., Krische, M. J., Lehn, J.-M., Eds.; Molecular Self-Assembly: Organic versus Inorganic Approaches, Vol. 96; Springer: New York, 2000; p 3. (g) Beijer, F. H.; Sijbesma. (h) Beijer, F. H.; Sijbesma, R. P.; Vekemans, J. A. M.; Meijer, E. W.; Kooijman, H.; Spek, A. L. *J. Org. Chem.* **1996**, *61*, 6371. (i) Whitesides, G. M.; Simanek, E. E.; Mathias, J. P.; Seto, C. T.; Chin, D. N.; Mammen, M.; Gordon, D. M. *Acc. Chem. Res.* **1995**, *28*, 37. (j) Lawrence, D. S.; Jiang, T.; Levett, M. *Chem. Rev.* **1995**, *95*, 2229.

(14) For reviews of hydrogen-bonding self-assembly, see: (a) McCullagh, M.; Tatiana, P.; Tonzani, S.; Winter, N. D.; Schatz, G. C. *J. Phys. Chem. B* **2008**, *23*, 105. (b) Bouteiller, L. *Adv. Polym. Sci.* **2007**, *207*, 79. (c) Datta, A.; Pati, S. K. *Chem. Soc. Rev.* **2006**, *35*, 1305. (d) Percece, V.; Ungar, G.; Peterca, M. *Science* **2006**, *313*, 55. (e) Ajayaghosh, A.; George, S. J.; Schenning, A. P. H. J. *Top. Curr. Chem.* **2005**, *258*, 83. (f) Bushy, M. L.; Nguyen, T.-Q.; Zhang, W.; Horoszewski, D.; Nuckolls, C. *Angew. Chem., Int. Ed.* **2004**, *43*, 5446. (g) Sherrington, D. C. *Chem. Soc. Rev.* **2001**, *30*, 83. (h) Lehn, J.-M. *Science.* **1996**, *295*, 2400. (i) Corbin, P. S.; Zimmerman, S. C.; Thiessen, P. A.; Hawryluk, N. A.; Murray, T. J. *J. Am. Chem. Soc.* **2001**, *123*, 10475. (j) Whitesides, G. M.; Mathias, J. P.; Seto, C. T. *Science.* **1991**, *254*, 1312.

Scheme 2. Chromophores for PVD Growth of NLO-Active Thin Films

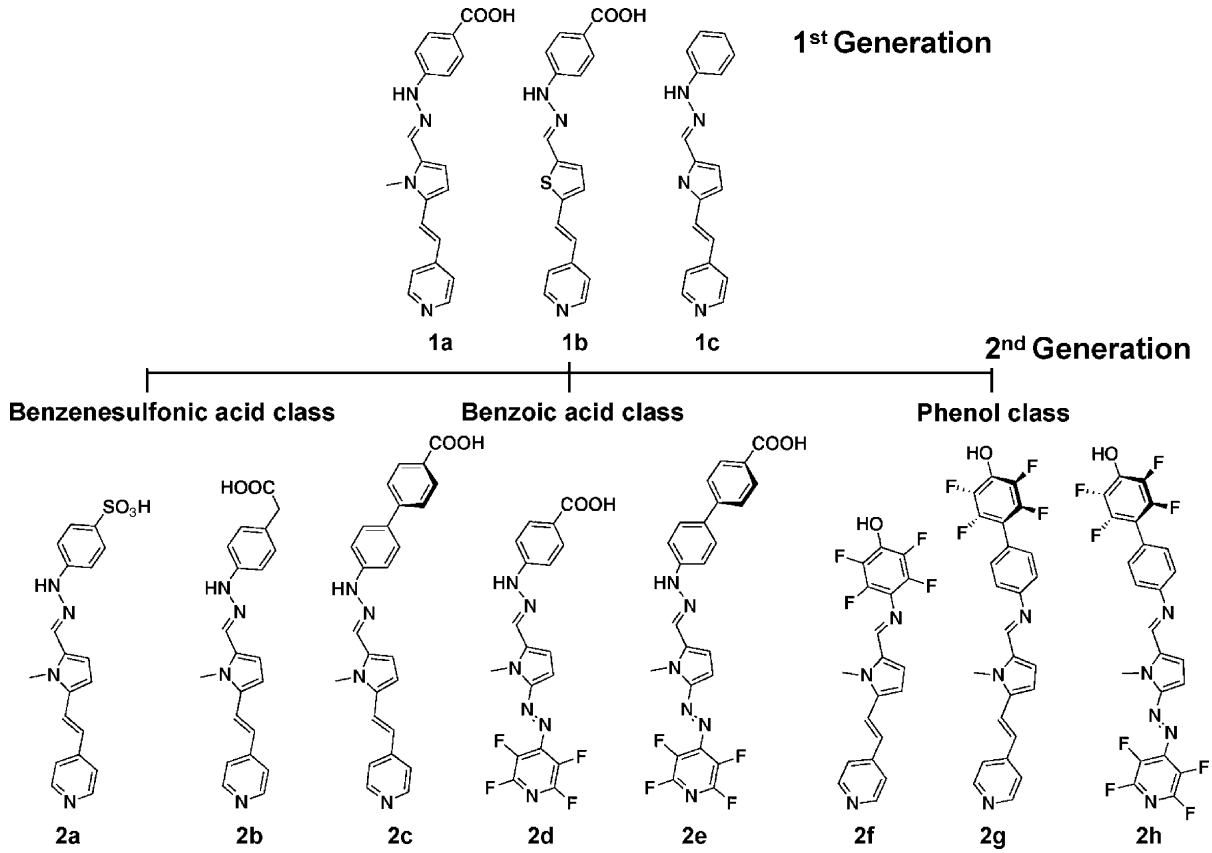

it should: (1) strengthen the intrinsic NLO response by enhancing electron accepting capability,[2] (2) enhance benzoic acidity, hence stabilizing hydrogen-bonding in chromophores such as **1a**,[13d] and (3) decrease chemical and thermal instability that frequently accompanies large-β chromophores having extended π systems and low-lying excited states.[15] Fluorine-rich NLO chromophores can exhibit high thermal stability, chemical inertness, low dielectric constants, and good NIR optical transparency.[16] To further increase intrinsic β response, conjugative decoupling was also implemented into "push−pull" backbones at the chromophore electron donor end (chromophores **2b**, **2c**, and **2g**). The strategy is to reduce electronic communication between electron-deficient hydrogen-bond donor and electron-rich chromophore electron donor substituents, thus enhancing charge availability for traditional push−pull response enhancement.[2] To address extrinsic (hydrogen-bond originating) response enhancement issues while seeking hydrogen-bonding candidates suited for directing acentric multilayer growth, three **1a** substituents were investigated: benzenesulfonic acid (*BzSO$_3$H*), perfluoropyridine (*FPy*), and perfluorophenol (*FPOH*). These substitutions allow probing of hydrogen-bonding-dependent response changes, primarily reflecting the hydrogen-bond donor acidity, which should tune the pyridyl charge deficiency.[11a]

In the progression from chromophore molecule to macroscopic film, intermolecular interactions are known to direct the noncentrosymmetry necessary for bulk NLO response.[1−3,17] Interactions such as $\pi-\pi$ stacking and intermolecular hydrogen-bonding may optimize intermolecular connectivities and film organization. In previous studies, intermolecular head-to-tail hydrogen-bonding interactions were shown to strongly enforce uniform acentric growth.[11a,b] Therefore, in the present chromophore design criteria, hydrogen-bonding motifs were imple-

(15) Galvan-Gonzalez, A.; Belfield, K. D.; Stegeman, G. I.; Canva, M.; Marder, S. R.; Staub, K.; Levina, G.; Twieg, R. J. *J. Appl. Phys.* **2003**, *94*, 756, and references therein.

(16) (a) Medina, M. B.; Beljonne, D.; Egelhaaf, H.-J.; Gierschner, J. *J. Chem. Phys.* **2007**, *126*, 111101. (b) Crouch, D. J.; Skabara, P. J.; Heeney, M.; McCulloch, I.; Coles, S. J.; Hurstshouse, M. B. *Chem. Commun.* **2005**, 1465. (c) Kim, Y.; Swager, T. M. *Chem. Commun.* **2005**, 372. (d) Salzner, U. *Curr. Org. Chem.* **2004**, *8*, 569. (e) Newman, R.; Frisbie, C. D.; da Silva Filho, D. A.; Brédas, J. L.; Ewbank, P. C.; Mann, K. R. *Chem. Mater.* **2004**, *16*, 4463. (f) Luo, J.; Haller, M.; Ma, H.; Liu, S.; Kim, T.-D.; Tian, Y.; Chen, B.; Jang, S.-H.; Dalton, L. R.; Jen, A. K.-Y. *J. Phys, Chem. B.* **2004**, *108*, 8523–8530. (g) Gurge, R. M.; Sarker, A. M.; Lahti, P. M.; Hu, B.; Karasz, F. E. *Macromolecules.* **1997**, *30*, 8286.

(17) (a) Zhang, C.-Z.; Lu, C.; Zhu, J.; Wang, C.-Y.; Lu, G.-Y.; Wang, C.-S.; Wu, D.-L.; Liu, F.; Cui, Y. *Chem. Mater.* **2008**, *20*, 4628. (b) Li, Q.; Sa, R.; Liu, C.; Wu, K. *J. Phys. Chem. A* **2007**, *111*, 7925. (c) Sullivan, P. A.; Rommel, H.; Liao, Y.; Olbricht, B. C.; Akelaitis, A. J.-P.; Firestone, K. A.; Kang, J.-W.; Luo, J.; Davies, J. A.; Choi, D. H.; Eichinger, B. E.; Reid, P. J.; Chen, A.; Jen, A. K.-Y.; Robinson, B. H.; Dalton, L. R. J. *J. Am. Chem. Soc.* **2007**, *129*, 7523. (d) Tang, Z.; Johal, M. S.; Scudder, P.; Caculitan, N.; Magyar, R. J.; Tretiak, S.; Wang, H.-L. *Thin Solid Films.* **2007**, *516*, 58. (e) Senechal-David, K.; Hemeryck, A.; Tancrez, N.; Toupet, L.; Williams, J. A. G.; Ledoux, I.; Zyss, J.; Boucekkine, A.; Guegan, J.-P.; Bozec, H. L.; Maury, O. *J. Am. Chem.* **2006**, *128*, 12243–12255. (f) Davidson, E. R.; Eichinger, B. E.; Robinson, B. H. *Opt. Mater.* **2006**, *29*, 360–364. (g) Balakina, M. Y.; Nefediev, S. E. *Comput. Mater. Sci.* **2005**, *38*, 467–472. (h) Keinan, S.; Ratner, M.; Marks, T. J. *Chem. Mater.* **2004**, *16*, 1848–1854. (i) Wu, K.; Snijders, J. G.; Lin, C. *J. Phys. Chem. B.* **2002**, *106*, 8954. (j) Jensen, L.; Astrand, P. O.; Osted, A.; Kongsted, J.; Mikkelsen, K. V. *J. Chem. Phys.* **2002**, *116*, 4001. (k) Maroulis, G. *J. Chem. Phys.* **2000**, *113*, 1813. (l) Moliner, V.; Escribano, P.; Peris, E. *New J. Chem.* **1998**, 387. (m) Reis, H.; Papadopoulos, M. G.; Munn, R. W. *J. Chem. Phys.* **1998**, *109*, 6828. (n) Di Bella, S.; Ratner, M. A.; Marks, T. J. *J. Am. Chem. Soc.* **1992**, *114*, 5842. (o) Kanis, D. R.; Marks, T. J.; Ratner, M. A. *Chem. Mater.* **1991**, *3*, 19–22.

mented to promote: (1) parallel dipolar alignment, and (2) unidirectional growth via appropriate hydrogen-bond pairing. To date, there have been no comprehensive experimental or theoretical studies of fluorinated chromophores in NLO thin-film PVD growth processes. Indeed, few experimental or modeling studies have examined structure-directing hydrogen-bonding effects in NLO systems.[11,17h]

In this contribution, combined computational and experimental approaches are employed to design, synthesize, and implement in PVD film growth, volatile hydrogen-bonding chromophores (Scheme 2) for large NLO response (β_{vec} and $\chi^{(2)}_{zzz}$) organic thin films. Density functional theory (DFT) is first used to predict molecular and intermolecular hydrogen-bonding geometries of chromophores **1a** and **2a**−**h**, to determine hydrogen-bonding stabilization energies (E_{sta}) for various pairing motifs, and to predict film growth patterns via computation on dimers and trimers, so as to better understand film $\chi^{(2)}_{zzz}$ response. Using the DFT-defined geometries, semiempirical INDO/S calculations are next employed to investigate linear optical properties and static hyperpolarizabilities (β_o) using a Sum-over-States (SOS) scheme. Computed molecular β_o's are found to be as large as 1400×10^{-30} esu, the largest predicted to date for a hydrogen-bonded NLO chromophore. For bulk response, cluster calculations are then used to simulate early film growth stages, so as to gain a clearer picture of the intermolecular interactions ($\pi-\pi$, head-to-tail) affecting multimolecular response. Target chromophores identified by the computation are then synthesized, characterized by appropriate physicochemical techniques, and implemented in PVD growth experiments. For PVD-derived thin films, we report detailed characterization by optical spectroscopy, AFM, and angle-dependent polarized SHG spectroscopy. It will be seen that the PVD-derived films of this chromophore series not only have responses exceeding 300 pm/V, but also offer film thermal stability, transparency, and acentric microstructure, along with the first computational evidence that chromophore architecture can be tailored to direct the early stages of chromophore growth and overall thin film NLO response.

Computational Methods

(a) Models. Using the Maestro interface, five structural models (Models 1−5 in Scheme 3) were constructed for this investigation. Initial chromophore monomeric geometries and hydrogen-bonding motifs were computed using Hartree−Fock implemented in the Jaguar[18] package within the Maestro interface. Models 1−5 were constructed from geometries minimized at the B3LYP/6-31G** level. Model 1 addresses intermolecular interactions and the stabilizing effects associated with each hydrogen-bonding motif (see results). EO response changes caused by hydrogen-bonding are accounted for in Model 2a. The purpose of this model is to estimate molecular response in the presence of hydrogen-bonding for comparison with thin films. For simplicity and minimal impact on response, hydrogen-bonding donor motifs were not used in this representation as was the case in Model 2b. Expanding the structural scope further, Models 2−4 were used to target structure-response relationships exhibited by dimers and trimers so as to investigate hydrogen-bonding influence on molecular alignment. Lastly, Model 5 explores possible intermolecular $\pi-\pi$ interactions involved in NLO film structures that offer a possible pathway for either centrosymmetric (depicted) or noncentrosymmetric growth.

(b) DFT Calculations. Using geometries obtained from the HF calculations, an option in the Jaguar[18] program, all non-hydrogen bonding monomers (as drawn in Scheme 2), H-donor···monomer (Model 2a), dimers (both parallel and antiparallel arrangement), and trimers were subjected to restricted geometry optimization using the B3LYP[19] DFT hybrid method with a 6-31G** basis as implemented in Jaguar.[18] To ensure that each structural model was actually energy minimized, global minima were located by minimizing dimer or trimer energetics, beginning from different mutual orientations of the component monomers. Depending on the particular chromophore system, parallel or antiparallel face-to-face alignment motifs were found to represent the lowest energy cluster structures. To explore dipole moment and response additivity in each of these Models, further adjustments were made (Schemes 3

Scheme 3. Structural Models Used for DFT-Energy Minimization, INDO/S Spectral Analysis, and SOS Hyperpolarizability Calculation for Chromophores **1a** and **2a**−**h**, and Their Corresponding Hydrogen Donors and Acceptors[a]

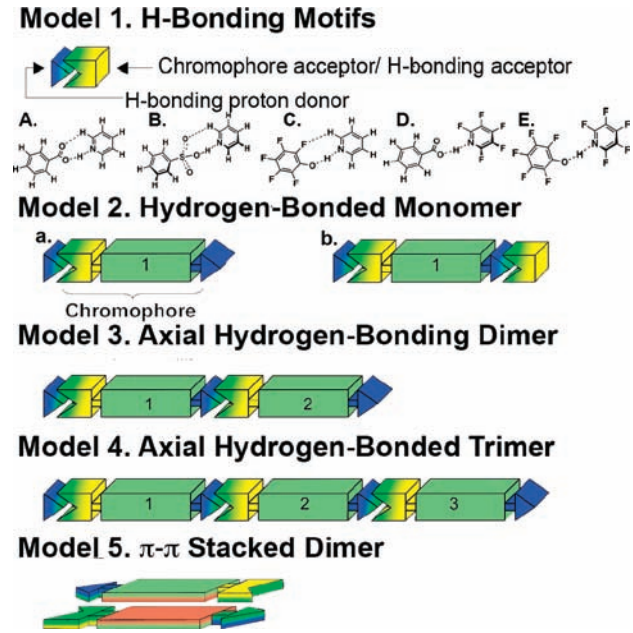

[a] Model 1 consists of structural combinations present in structural scenarios **A**−**E**. Model 2 uses hydrogen-bonding to examine hydrogen-bonding affects explore extrinsic molecular properties. Models 3 and 4 focus on response addivity and hydrogen-bonding dependent growth control, while Model 5 explores parallel and anti-parallel dimer face-to-face stacking effects. Models are explained in greater detail in the Theoretical section.

Table 1. Experimental and Computed Optical Absorption Data for Chromophores **1a** and **2a**−**h**

	absorption (nm)					
	experimental			calculated[a]		
chromophore	DMSO solution (λ_{max})	film (λ_{max})[b]	$\Delta\lambda$[c]	monomer	model **2a**[d]	$\Delta\lambda$[e]
1a	325, 428	440	12	382	388	6
2a	348, 443, 531	362	−81	389	566	177
2b	325, 438	—[f]	—[f]	388	396	8
2c	346, 454	366	−88	392	380	−12
2d	348, 568	547	−21	455	446	−9
2e	366, 588	551	−37	471	452	−19
2f	402	429	17	378	400	22
2g	407	409	2	380	383	3
2h	474	574	100	413	440	27

[a] Results of INDO/S semiempirical analysis. [b] 100 nm thick films. [c] $\Delta\lambda = \lambda^{F}_{max} - \lambda^{S}_{max}$. [d] Donor-H···chromophore where donor is either benzoic acid, benzene sulfonic acid, or perfluorophenol. [e] $\Delta\lambda = \lambda^{chrom}_{max} - \lambda^{mono}_{max}$. [f] Thermal degradation accompanies film growth for chromophore **2b**.

(18) *Jaguar 4.2*; Schrödinger, Inc.: Portland, OR, 1991−2000.

(19) (a) Becke, A. D. *Phys. Rev. A* **1988**, *38*, 3098. (b) Lee, C.; Yang, W.; Parr, R. G. *Phys. Rev. B* **1988**, *37*, 785.

Scheme 4. General Chromophore Cluster Packing Sketch Showing Geometrical Parameters Used for Describing Packing and Bulk Response (β) as a Result of the Hydrogen-Bonding Interactions Specific to Each Molecule[a]

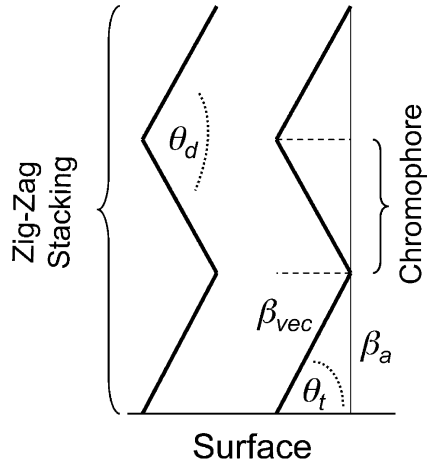

[a] θ_d is the angle between adjacent chromophore molecular long axes. θ_t is the molecular orientation angle with respect to the surface defined as $\theta_t = (1/2)\theta_d$ (see Model 2a). β_{vec} and β_a are the molecular long and adjusted hyperpolarizabilities, respectively. β_{vec} is the computed response determined using Model 2a which allows the calculation of β_a from the expression $\beta_a = \beta_{vec} \sin \theta$. Note that $3\beta_a \approx$ cluster response given by Model 4 (Scheme 3).

and 4). In Scheme 3, Models 2−4 use a hydrogen-donor motif (located at left) so that the computed response is solely dependent on alignment and not on differences in hydrogen-bonding within the clusters. Furthermore, since chromophores tend to organize in a "zig-zag" pattern, steps were taken to compute loss in molecular response due to this alignment characteristic (Scheme 4). Here, a correction for response is calculated using θ_t (Scheme 4), which decreases the effective response in each molecule. This is accounted for using SOS since it is calculated along the molecular axis or cluster axis. Additionally, θ_d (axial−axial dimer hydrogen-bonding angle), a hydrogen-bond specific term, gives the angle formed between adjacent molecules.

(c) Semiempirical INDO/S[20] CI Calculations. Semiempirical calculations employing the INDO/S[20] model developed by Zerner and co-workers were performed using the CNDO[21] program. An active space of 70 + 70 was used. All chromophores were studied as monomers and using structural Models 2−5. INDO/S provides the linear optical spectroscopic properties and excitations which are necessary input for hyperpolarizability calculations.

(d) Hyperpolarazibility (β) Calculations. From the INDO/S[20] output, the Sum-over-States[22] (SOS) approach was implemented to evaluate the nonlinear response (β) of the chromophores and chromophore clusters; the states involved came from a 70 + 70 set of single excitations.[17o] The first hyperpolarizability (β) appears as the third rank tensor in the first nonlinear term that arises in the dependence of the molecular induced dipole moment (μ) on the applied electric field F experienced by the molecule:[1]

$$\mu_i = \mu_i^{(0)} + \sum_i \alpha_{ij} F_j + (^1/_2) \sum_{j,k} \beta_{ijk} F_j F_k \qquad (1)$$

Here $\mu_i^{(0)}$ is the permanent dipole moment of the molecule in direction i, F_j is the component of the electromagnetic field in direction j, and α and β are the static (zero frequency, $\omega = 0.0$ eV) first- and second-order polarizability tensors. We concentrate here on β. To avoid issues of resonance enhancement, we report only the limiting zero frequency or "static" case ($\omega = 0.0$ eV). We are interested in the β_μ (β_{vector}) component of the β tensor (eq 2):

$$\beta_\mu = \frac{\sum_{i=x,y,z} \beta_i \mu_i}{\mu}, \qquad \beta_i = \frac{1}{3} \sum_{k=x,y,z} (\beta_{ikk} + \beta_{kik} + \beta_{kki}) \qquad (2)$$

In addition to β, we calculated molecular and molecular cluster dipole moments to examine addivity. This INDO/SOS scheme has demonstrated an ability to predict with reasonable accuracy the linear optical and NLO response properties of diverse organic chromophore classes.[2a,r−17h]

Results

First, the synthesis of eight push−pull hydrogen-bonding chromophores is described in detail. Each new chromophore was fully characterized via conventional analytical/spectroscopic techniques, and volatility as well as thermal stability were assessed by thermogravimetric analysis (TGA). Chromophore linear optical properties were next analyzed using optical absorption spectroscopy. In addition to solution phase chromophore characterization, thin films were then grown via vacuum physical vapor deposition (PVD) and analyzed by various physical techniques, including optical absorption spectroscopy and AFM. Finally, angle-dependent polarized SHG spectroscopy is used to measure bulk NLO response and polar regularity as a function of growth conditions and film thickness.[11a,b,23] To understand each of these systems at the molecular level and their microstructures in thin films, theoretical analyses are also performed. These systems rely on acentric organization directed primarily by hydrogen-bonding, and computation proves highly informative in understanding molecular NLO response. Methodologies include DFT, INDO/S,[20] and SOS[22] formalisms to predict molecular structure, favorable organization patterns, and chromophore hyperpolarizabilities (β). Furthermore, cluster calculations on molecular packing motifs as a function of hydrogen-bonding differences were implemented to assess their impact on molecular response additivity.

Chromophore Design, Synthesis, Characterization. Synthetic routes to present chromophores are summarized in Schemes 5−7. The syntheses of the eight subject chromophores can be divided into three structural component categories: (a) chromophore electron-donor/hydrogen-bond donor segments (Scheme 5), (b) chromophore backbone/electron-acceptor/hydrogen-bonding acceptor segments (Schemes 6 and 7), and (c) chromophore electron-acceptors (Schemes 6 and 7). With the goal of increasing the electron richness of the chromophore precursor donor amine groups, by insulating from other parts of the molecules, two conjugative "decoupling" approaches were taken. The first approach utilized a twisted-biaryl motif as in chromophores **2c**, **2e**, **2g** and **2h**. For synthesizing **3** in one pot, the lithium salt of 2,3,5,6-tetrafluoroanisole was stannylated using tributyltin chloride to afford reagent **1** in 84% yield (Scheme 4). Next, **1** and 4-iodoaniline were coupled via a Stille cross-coupling using a Pd/CuI/triphenylarsine catalyst to generate sterically encumbered biaryl **2** in high yield. Subsequent deprotection of anisole **2** using BBr_3 led to complete conversion

(20) Ridley, J.; Zerner, M. *Theor. Chim. Acta* **1973**, *32*, 111.
(21) Zeng, J.; Hush, N. S.; Reimers, J. R. *J. Am. Chem. Soc.* **1996**, *118*, 2059.
(22) Orr, B. J.; Ward, J. F. *Mol. Phys.* **1971**, *20*, 513.
(23) (a) Yamada, S.; Lee, I.-Y. L. *Anal. Sci.* **1998**, *14*, 1045. (b) Forrest, S. R. *Chem. Rev.* **1997**, *97*, 793. (c) Shen, Y. R. *Ann. Rev. Phys. Chem.* **1989**, *40*, 327.

Scheme 5. Synthetic Routes to Hydrogen-Bond Donating Groups[a]

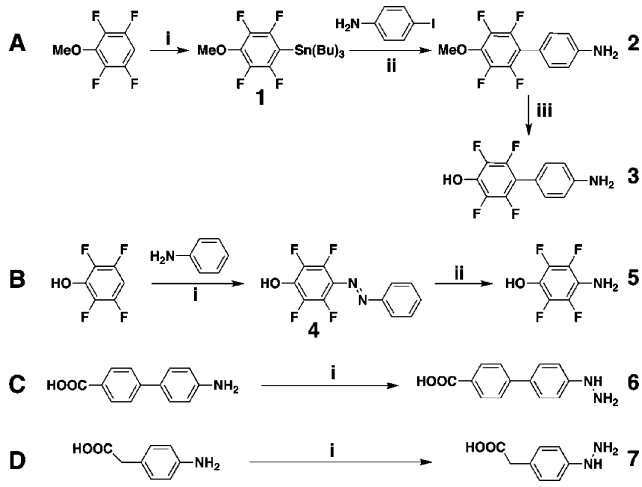

[a] Reaction Conditions: A. (i) *n*-BuLi, $(Bu)_3SnCl$, Ether, −78 °C; (ii) $IC_6H_6NH_2$, Pd(C), CuI, $AsPh_3$, CH_3CN; (iii) BBr_3, CH_2Cl_2. B. (i) $C_6H_5NH_2$, $NaNO_2$, HCl, NaOH; (ii) $Na_2S_2O_4$. C and D. (i) $NaNO_2$, $SnCl_2$, HCl, NaOH.

Scheme 6. Synthetic Routes to Chromophores **2a**, **2b**, **2c**, **2f**, and **2g** Using a Pyridyl Hydrogen-Bond Acceptor[a]

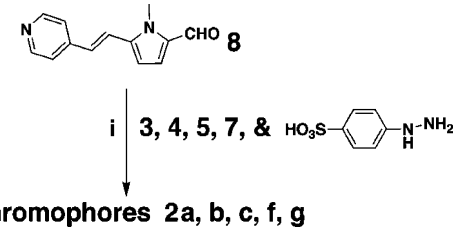

[a] Conditions: (i) **3**, **4**, **5**, **7**, or $HO_3SC_6H_4NHNH_2$, EtOH, reflux.

Scheme 7. Synthetic Route to Chromophores **2d**, **2e**, and **2h** Using the Perfluoropyridyl Hydrogen-Bond Accepting Group[a]

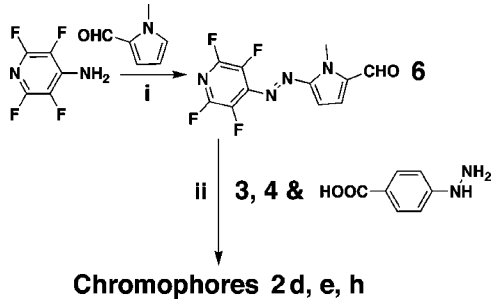

[a] Conditions: (i) $NaNO_2$, 48% HF; (ii) **3**, **4**, or $C_7H_8N_2O_2$, EtOH, reflux.

to alcohol **3** in 65% yield. For comparison, a "non-decoupled" version **5** was synthesized in two steps where 2,3,5,6-tetrafluoroanisole and aniline were coupled via diazotization to afford **4** which was immediately reduced. To provide similar decoupling in the carboxylic acid of **1a**, two approaches were taken. First a biaryl twisted precursor similar to **5** was synthesized via one-pot diazotization/reduction of 4′-amino-biphenyl-4-carboxylic acid using $NaNO_2$ and $SnCl_2$ to afford **6** in 77.2% yield. Using the same two-step amine-to-hydrazine conversion, 4-aminobenzeneacetic acid was also converted to reagent **7** in 42% yield. This hydrazine derivative allows the study of electronic "decoupling" using a methylene spacer instead of the biaryl twist of **3** and **6**.

The last of the chromophore precursor molecules required the synthesis of two pyridyl-pyrrole acceptor/backbone fragments differing by the presence of fluorine substituents (Schemes 6 and 7). The synthesis of *N*-methyl-pyrrole-2-carboxylaldehyde (**8**), the nonfluorinated version, has been reported elsewhere.[9a] The fluorinated version, **6**, was synthesized in one step. Thus, 4-amino-2,3,5,6-tetrafluoropyridine was converted to the intermediate diazonium fluoride salt in 48% HF. This product was then regioselectively coupled at the 2 position of 1-methylpyrrole-2-carboxyaldehyde to afford **6** in 68% yield.

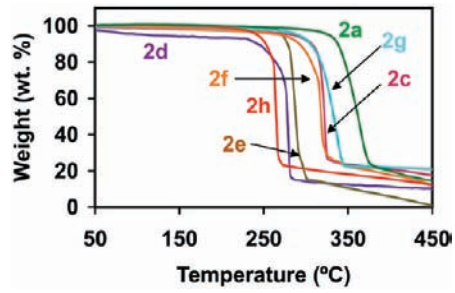

Figure 1. Thermogravimetric analysis of chromophores **2a** (green), **2c** (maroon), **2d** (purple), **2e** (brown), **2f** (orange), **2g** (teal), and **2h** (red). Temperature ramp = 1.5 °C min^{-1}; pressure = 0.01 Torr N_2.

Chromophores **2a**−**h** were all synthesized using conventional condensation chemistry involving reflux in absolute ethanol. Typically, the appropriate aldehyde and amine precursors afforded the target chromophores in high yield and purity. Combinations of the aforementioned precursors, in addition to 4-hydrazinobenzoic acid and 4-hydrazinobenzenesulfonic acid hemihydrate, were used in stoichiometric quantities to afford chromophores **2a**−**h** in acceptable yields. All new chromophores and their precursors were characterized by conventional analytical/spectroscopic techniques including ^1H and ^{19}F NMR spectroscopy, mass spectroscopy, and elemental analysis (see Supporting Information for details).

Chromophore Volatility and Thermal Stability. Thermogravimetric analysis (TGA) data (Figure 1) show clean to near-clean sublimation characteristics for all of the present chromophores at 0.01 Torr N_2, with <20% weight retention, demonstrating sufficient volatility and thermal robustness for vacuum PVD growth (performed at even lower pressures ∼2.5 × 10^{-6} Torr). Chromophore **2e** was found to be least volatile, presumably reflecting the strong hydrogen-bonding capacity, while highly fluorinated **2h** is most volatile. As for the remaining systems, chromophores containing perfluoropyridine (*FPy*), **2d** and **2e**, are more volatile (and soluble) than *FPOH*-containing molecules **2f** and **2g**. Whereas chromophore **2c** (T_{sub} ≈ 324 °C, the temperature corresponding to weight retention midpoint for sublimation) displays thermal stability similar to that of parent **1a** (T_{sub} ≈ 319 °C),[9a] chromophore **2a**, due to stronger hydrogen-bonding interactions, resists sublimation while still exhibiting significant thermal stablility (T_{sub} ≈ 355). The TGA plots do not include chromophore **2b** due to its thermal instability (T_d ≈ 180 °C) and marginal sublimation characteristics with ∼75% weight retention.

Chromophore and Film Linear Optical Characterization. Optical spectroscopy was used here to compare the optical characteristics of chromophores **1a** and **2a**−**h** in DMSO solution (Figure 2A) and as thin vapor-deposited films (Figure 2B; data are summarized in Table 1). For solution phase optical spectroscopy, the hydrogen-bond disrupting solvent DMSO was found necessary to obtain acceptable solubilities.[24] Depending

(24) Winstanley, K. J.; Smith, D. K. *J. Org. Chem.* **2007**, *72*, 2803.

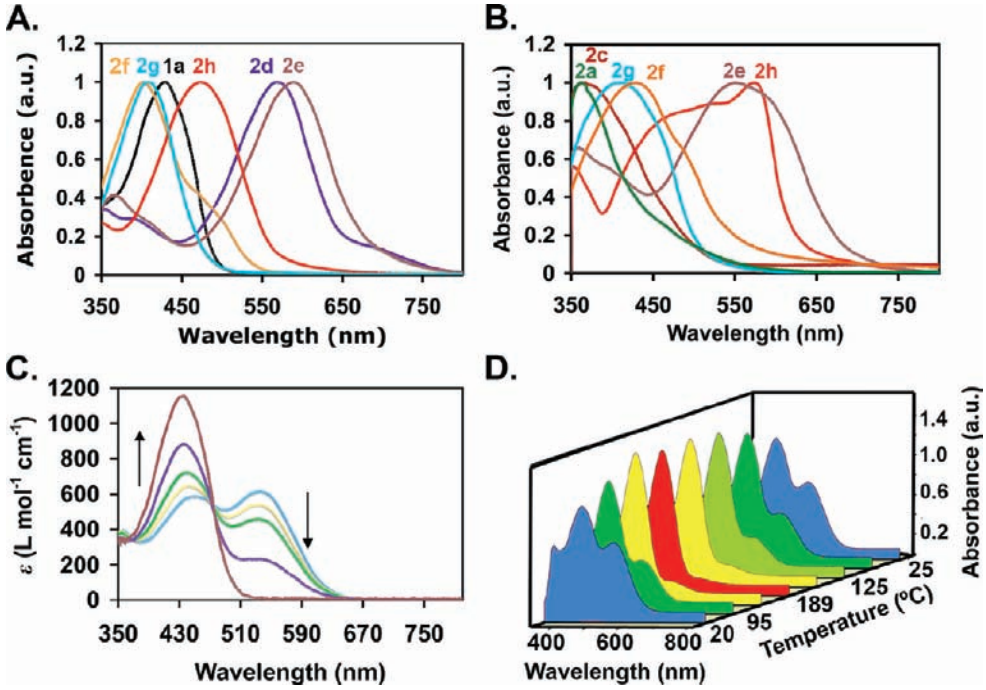

Figure 2. (A) Optical absorption spectra of the indicated chromophores in DMSO solution. (B) Optical absorption spectra of the indicated chromophores as 100 nm films. (C) Concentration-dependent optical absorption spectra of **2a** in DMSO solution. The arrows indicate changing of monomer and aggregate bands upon decreasing the concentration from 1.28×10^{-3} to 1.73×10^{-4} M. (D) Temperature-dependent optical absorption spectra of chromophore **2a** as a 1.28×10^{-3} M DMSO solution. Blue (cool) to red (hot) color transition signifies temperature change in the DMSO solution and the associated changes in monomer and aggregate bands.

on the particular chromophore, spectra generally exhibit strong $\pi-\pi^*$ charge-transfer (CT) excitations, from 402−588 nm, with additional weak low-energy excitations (e.g., Figure 1A, chromophores **2h**, **d**, and **e**). As expected, comparisons with the parent chromophore **1a** revealed both bathochromic ($\Delta\lambda_n^+$)[25] and hypsochromic ($\Delta\lambda_n^-$)[25] spectral shifts depending on the specific hydrogen-bonding motif. Further modifications, via hydrogen-bonding donor/electron−donor decoupling (e.g., **2c**), revealed small to moderate $\Delta\lambda_n^+$ values, typical of an increase in intramolecular charge transfer.[26]

Noticeable broadening of the optical spectral features is observed on going from the solution to film phase for most molecules. Modification of substitents and D−A decoupling impact film and solution absorption spectra differently, with the exception of all *FPy*-containing chromophores which exhibit characteristic $\Delta\lambda_n^+$ patterns unless doubly fluorinated (**2h**).[25] In general, $\Delta\lambda_n^-$ spectral shifts accompany the solution to film transition. One reason may be packing effects that alter chromophore geometries and intermolecular interactions. In addition to the usual optical spectral features (Figures 2A and B), a third broad shoulder was observed in chromophore **2a** solutions at higher concentrations (Figure 2C). This is ascribed to aggregation, supported by the systematics of the concentration- and temperature-dependent absorption spectra (Figure 2C and D).[27] Here, significant optical spectral changes are observed upon varying the concentration from 1.28×10^{-3} to 1.73×10^{-4} M, revealing an increase of the 443 nm ($\varepsilon = 1180$ L mol^{-1} cm^{-1}) CT band intensity and a concomitant diminution of the 531 nm band upon dilution. The well-defined isosbestic point is clearly suggestive of aggregation equilibria.[2a,27] This aggregation tendency is reasonable considering the acidity of the *BzSO$_3$H* group and its nonplanar geometry (Figure 3A). Furthermore, increasing the temperature of **2a** DMSO solutions from 25 to 189 °C and back down to 20 °C reveals reversible spectral feature changes in accord with aggregation equilibria (Figure 2D). Compared to DMSO solutions, the absorption maxima of 100 nm **2a** films (Figure 2B) exhibit further blue-shifting to ∼362 nm. This film blue-shifting tendency was also observed for chromophores **2c**, **2d**, and **2e** (Figure 2A and B, Table 1).

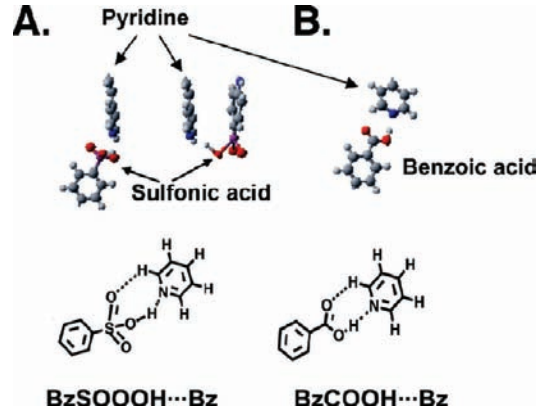

Figure 3. DFT-computed hydrogen-bonded fragments and the corresponding Chemdraw structures. (A) Two potential scenarios that may occur due to the three-dimentional nature of the sulfonic acid motif versus (B) the typical pairwise hydrogen-bonding structures between benzoic acid and pyridine.

(25) Either $\Delta\lambda_n^+$ or $\Delta\lambda_n^- = (\lambda_{max})_n = (\lambda_{max})_{2ndGen} - (\lambda_{max})_{\mathbf{1a}}$ is defined as the difference between the ICT band value of either 2nd generation chromophore and that of **1a** so to illustrate the influence of a particular hydrogen-bond motif change.

(26) Katritzky, A. R. *Handbook of Heterocyclic Chemistry*; Pergamon Press: Oxford, 1983.

(27) Dipolar molecule aggregation in solution is most frequently studied by optical spectroscopy: Würthner, F.; Yao, S.; Debaerdemaeker, T.; Wortmann, R. *J. Am. Chem. Soc.* **2002**, *124*, 9431.

Table 2. Nonlinear Response Characteristics for Films of Chromophores **1a** and **2a**−**h** from SHG Spectroscopy and Calculations

	$\chi^{(2)}_{zzz}$(pm/V)[a]		β(× 10^{-30} esu)			
chromophore	100 nm (D.S.)[b]	5 nm (S.S.)[c]	monomer	model 2a[d]	$\Delta\beta$[e]	tilt angle (Ψ)[f]
1a	20.6	20.6	22.1	25.6	3.50	49.0
2a	11.9	302	33.4	1407	1370	−
2b	−[g]	−[g]	24.7	104	79.3	−
2c	24.1	24.1	23.1	37.2	14.1	48.5
2d	155[h]	155[h]	177	153	−24.0	45.1
2e	46.2	46.2	238	141	−97.0	45.8
2f	15.2	33.2	33.4	75.6	42.2	43.9
2g	10.8	16.3	28.1	35.8	7.7	43.4
2h	19.8	40.2	172	130	−42.0	42.8

[a] Calibrated against quartz (nonlinear optical coefficient, $d_{11} = 0.45$ pm V^{-1}) at 1064 nm; uncertainties ± 10%. [b] Double-sided (∼100 nm total) films grown on glass substrates. Differences in $\chi^{(2)}_{zzz}$ arise from nonideal growth as in Figure 6B. [c] Single-sided (∼5 nm) films grown on glass substrates. Differences in $\chi^{(2)}_{zzz}$ arise from nonideal growth as in Figure 6B. [d] Computed molecular response using Model 2a (Scheme 3, donor-H···Chromophore) representing theoretical molecular film response. [e] $\Delta\beta = \beta_{\text{Model2a}} - \beta_{\text{mono}}$, change in response for each molecule due to hydrogen-bonding. [f] Estimated from $\chi^{(2)}_{zzz}/\chi^{(2)}_{zyy} = 2\cot^2\Psi$, making the usual assumptions.[9c] [g] Thermal degradation accompanies film growth for chromophore **2b**. [h] Response may have resonance enhancement contribution due to proximity of λ_{max} to frequency doubled light at 532 nm.

Film Electrooptic and Microstructure Characterization. Polarized angle-dependent second harmonic generation (SHG) spectroscopic measurements were carried out on films of chromophores **2a** and **2c**−**2h** grown on clean glass substrates at $\lambda_0 = 1064$ nm in the transmission mode. Measurements were carried out on specimens having films grown on one or both sides of the glass substrates. Double-sided samples were fabricated with 50 nm thick films, giving a total chromophore film thickness of 100 nm, while single-sided samples were fabricated with films varying in thickness from a few nm to over 1.0 μm. From these samples, two vital pieces of information were provided by SHG spectroscopy, the quadratic susceptibility ($\chi^{(2)}_{zzz}$) and thickness-dependent response ($I^{2\omega}$)$^{1/2}$.[11,23] Individual thin film bulk responses ($\chi^{(2)}_{zzz}$) were obtained by calibrating the angle-dependent SHG data against a quartz reference, yielding responses ranging from 11.9 to 302 pm/V at $\omega = 1064$ nm for films of chromophores **1a** and **2b**−**2h**. This range is highly dependent on the intrinsic molecular structure characteristics of the chromophores, their likely packing motifs, and thin film growth characteristics dictated by these factors (see more below). Data are compiled in Table 2. Typical SHG interference patterns[7−11] from glass substrates coated on both sides with a chromophore thin film are shown in Figure 4. A key metric evident in Figure 4 indicating high film quality and uniformity, is the presence of near-zero intensity minima in the interference patterns for films grown on both sides of the glass substrates.[28] Assuming a unidimensional chromophore (e.g., with a single dominant β tensor component) and minimal dispersion, the average orientation angle of the chromophore dipoles with respect to the surface normal (tilt angle) can then be calculated from the expression $\chi^{(2)}_{zzz}/\chi^{(2)}_{zyy} = 2\cot^2\Psi$.[9c] The average tilt angles for the present self-assembled chromophoric superlattices fall in the range of $\Psi = 42.8-49.0°$ with pyridine-containing chromophores exhibiting slightly greater angles than those containing fluorine substituents (Table 2). Table 2 summarizes the bulk second-order nonlinear susceptibilities ($\chi^{(2)}_{zzz}$) for films of chromophores **1a** and **2a**−**h**, and computed hyperpolarizabilities (β) using the corresponding monomer and Model 2a (Scheme 3) structures (see more below).

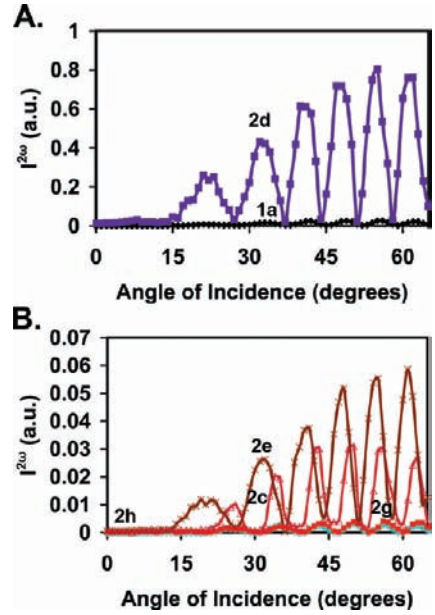

Figure 4. Angle-dependent second harmonic generation spectra of films of the indicated chromophores, deposited at equal thicknesses on both sides of glass substrates: (A) **2d** (purple) versus **1a** (black) showing both the contribution of resonance enhancement and the effects of the stronger perfluoropyridine acceptor. (B) Comparison of the response of films of chromophores **2c** (maroon), **2e** (brown), **2g** (teal), and **2h** (red).

As for response dependence on film thickness, as noted above, single-sided films of chromophores **1a** and **2a**−**h** were studied to assess the uniformity and persistence of mictrostructural acentricity as a function of growth thicknesses (up to 1.0 μm). It is found that the ($I^{2\omega}$)$^{1/2}$ dependence on film thickness depends principally on the particular hydrogen-donating motif. Thus, chromophores bearing *BzCOOH* (benzoic acid) groups exhibit linear ($I^{2\omega}$)$^{1/2}$ response with thickness (Figure 5A; films of chromophores **2c**, **2d**, and **2e**) after correction for self-absorption.[11a] Thus, $\chi^{(2)}_{zzz}$ remains uniform with film thickness while achieving the largest response reported to date for an organic vapor-deposited NLO film, $\chi^{(2)}_{zzz} \approx 155$ pm/V (chromophore **2d**). However, due to the hydrogen-bonding related hypsochromic optical effects noted above, the 542 nm λ_{max} is proximite to the frequency-doubled 532 nm fundamental light ($I^{2\omega}$), suggesting a resonant contribution[1e,29] to the response.

In regard to films of chromophores bearing either *BzSO$_3$H* (sulfonic acid, **2a**) or *FPOH* (tetrafluorophenol, **2f**−**2h**) substituents, the ($I^{2\omega}$)$^{1/2}$ SHG signals saturate with increasing film thickness, even after correcting for self-absorption in thicker samples (Figures 5B and 6). Saturation of ($I^{2\omega}$)$^{1/2}$ is generally observed at film thicknesses of 250−500 nm, where film quality decreases and haziness becomes visible. The exception is chromophore **2a** which shows complete response loss after only

(28) (a) Simpson, G. J.; Rowlen, K. L. *J. Am. Chem. Soc.* **1999**, *121*, 2635. (b) Yitzchaik, S.; Roscoe, S. B.; Kakkar, A. K.; Allan, D. S.; Marks, T. J.; Xu, Z.; Zhang, T.; Lin, W.; Wong, G. K. *J. Phys. Chem.* **1993**, *97*, 6958. (c) Kajzar, F.; Messier, J.; Zyss, J.; Ledoux, I. *Opt. Commun.* **1983**, *45*, 133. (d) Bloembergen, N.; Pershan, P. N. *Phys. Rev.* **1962**, *128*, 606.

(29) (a) Bruno, V.; Castaldo, A.; Centore, R.; Sirigu, A.; Sarcinelli, F.; Casalboni, M.; Pizzoferrato, R. *J. Polymer Sci. A* **2002**, *40*, 1468. (b) Pellegrini, V.; Colombelli, R.; Carusotto, I.; Beltram, F. *Appl. Phys. Lett.* **1999**, *74*, 1945.

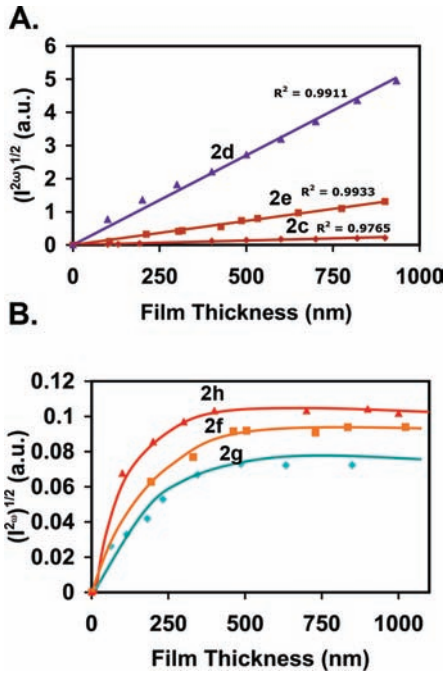

Figure 5. Square-root of SHG response as a function of vapor-deposited film thickness: (A) for chromophores **2c** (maroon), **2e** (brown), **2d** (purple) and (B) chromophores **2h** (red), **2g** (teal), and **2f** (orange). The SHG responses of films of chromophores **2c**, **2e**, and **2d** are each corrected for self-absorption at 532 nm using the equation $I_0^{2\omega} = I_0^{2\omega}\, e^{(\alpha l/4)((\alpha l/4)}\, \sinh(\alpha l/4)$, where α is the extinction coefficient at 532 nm (α = 0.000947 (**2c**), 0.00871 (**2e**), and 0.0148 nm^{-1}(**2d**)) and l is the film thickness.[11a] Resonance enhancement presumably plays a role in increasing response in films of **2d**. Films of **2f**−**2h** show nonlinear growth as a function of film thickness.

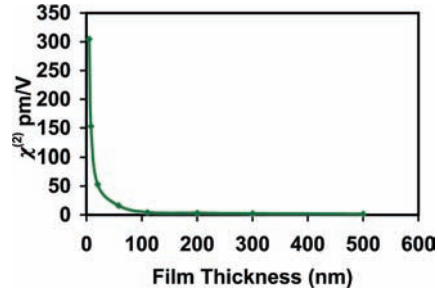

Figure 6. Decrease in $\chi^{(2)}$ for vapor-deposited **2a** films as a function of film thickness up to 500 nm.

a few nm thickness (Figure 6). Nevertheless, molecular structure-dependent response variations (e.g., from fluorination π-system conjugative decoupling) are clearly evident in the data (Figure 5A). Chromophore **2a**, with the greatest Brønsted acidity and thus greatest potential proton donation for pyridyl charge development, yields the largest observed $\chi^{(2)}_{zzz}$ response of all of the present thin films, ~302 pm/V for films <10 nm thick. However at thicknesses greater than 10 nm, **2a** exhibits a precipitous fall in response (Figure 6), suggesting the onset of centrosymmetric growth.[30]

Tapping-mode AFM measurements were performed on 100 nm films of each chromophore. Representative images for films of chromophores **2a**, **2c**, **2d**, **2e**, **2f**, and **2g** are shown over 5.0 × 5.0 μm scan areas (Figure 7). The images reveal increased grain texture and rms surface roughness, from 0.101 nm to 15.7 nm on going from films of *BzSO$_3$H* and *BzCOOH* chromophore derivatives to films of *FPOH* derivatives. This increase in roughness parallels the pronounced loss of acentric order observed in the *FPOH* $(I^{2\omega})^{1/2}$ vs thickness plots (Figure 5B), and the accompanying loss of visual transparency at thicknesses greater than ~250 nm.

In addition to optical spectroscopy, SHG, and AFM as microstructural characterization tools, X-ray diffraction experiments were also carried out on the present hydrogen-bonded chromophore films. Conventionally, Θ−2Θ diffraction scans are utilized to obtain out-of-plane *d*-spacings, molecular orientations relative to the substrate surface, and information on long-range film microstructural order.[12b,31] In the present case, Θ−2Θ scans of **2a**−**h** films varying considerably in thicknesses afford no obvious specular features indicative of long-range microstructrual order.

Theoretical Calculations. Computational studies of NLO chromophore response are common in the literature,[1,2,17] and several investigations have focused on variations in hyperpolarizability (β) induced by weak intermolecular interactions such as hydrogen-bonding. Examples include simple "models" such as water dimers[17k] or a linear array of HF molecules,[17l] while other studies have focused on the urea crystal structure[17i,m] or *para*-nitroaniline dimers.[17n,l] These investigations reveal that several factors underlie hyperpolarizability changes observed on proceeding from monomers to dimers or clusters. These factors include hydrogen-bonding interactions (strength and separation), and relative molecular dipole moment orientations (response additivity). However, few modeling studies have dealt with hydrogen-bonded organic chromophores, and response changes arising from structure-directing intermolecular hydrogen-bonding employed in designs for NLO film self-assembly.[17h] The approach in the present work is to use experimental and computational tools in tandem.[9b,17e] For the latter, we employed DFT and semiempirical methods to analyze molecular systems which depend on intermolecular hydrogen-bonding, substituent location, and conjugative decoupling for both NLO response and acentric organization. To enhance monomer *intrinsic* response, this study employed two tactics: (1) chromophore electron-donor/hydrogen-bonding donor disruption via biaryl twisting and (2) strengthening of electron-accepting capacity by introduction of electronegative fluorine. For conjugative disruption between chromophore electron-rich electron donors (e.g., the secondary amine in chromophore **1a**) and hydrogen-bond donors (e.g., benzoic acid), either methylene or a twisted biaryl (**2c**) bridges were used to enhance charge localization on the secondary amine. As for hydrogen-bonded oligomers (Model 2a) of chromophores **1a** and **2a**−**h**, studies were performed to probe the *extrinsic* influence on β of various hydrogen-bonding motifs, from simple molecular pairs through larger multimolecular clusters where molecular response additivity is scrutinized (see Scheme 3). Important aspects investigated include: (a) acid−base stabilization energy (E_{sta}), (b) changes in both λ_{max} and β for non- or hydrogen-bonded monomers, and (c) additivity effects on dipole moment (μ) and β in the progression from monomers to trimers. Structural analyses were performed at the DFT/B3LYP/6-31G** level, while optical spectroscopic and β responses, based on these geometries, were obtained at the INDO/S and SOS levels, respectively.

(30) Wang, G.; Kiehne, G. T.; Wong, G. K. L.; Ketterson, J. B.; Liu, X.; Chang, R. P. H. *Appl. Phys. Lett.* **2002**, *80*, 401.
(31) (a) *Elements of X-Ray Diffraction*, 3rd ed.; Cullity, B. D., Stock, S. R., Eds.l Prentice Hall: New Jersey, 2001. (b) *Diffraction from Materials*, 2nd ed.; Schwartz, L. H., Cohen, J. B., Eds.; Springer-Verlag: Berlin. (c) *The Basics of Crystallography and Diffraction*; Hammond, C., Ed.; Oxford University Press: Oxford, 1997.

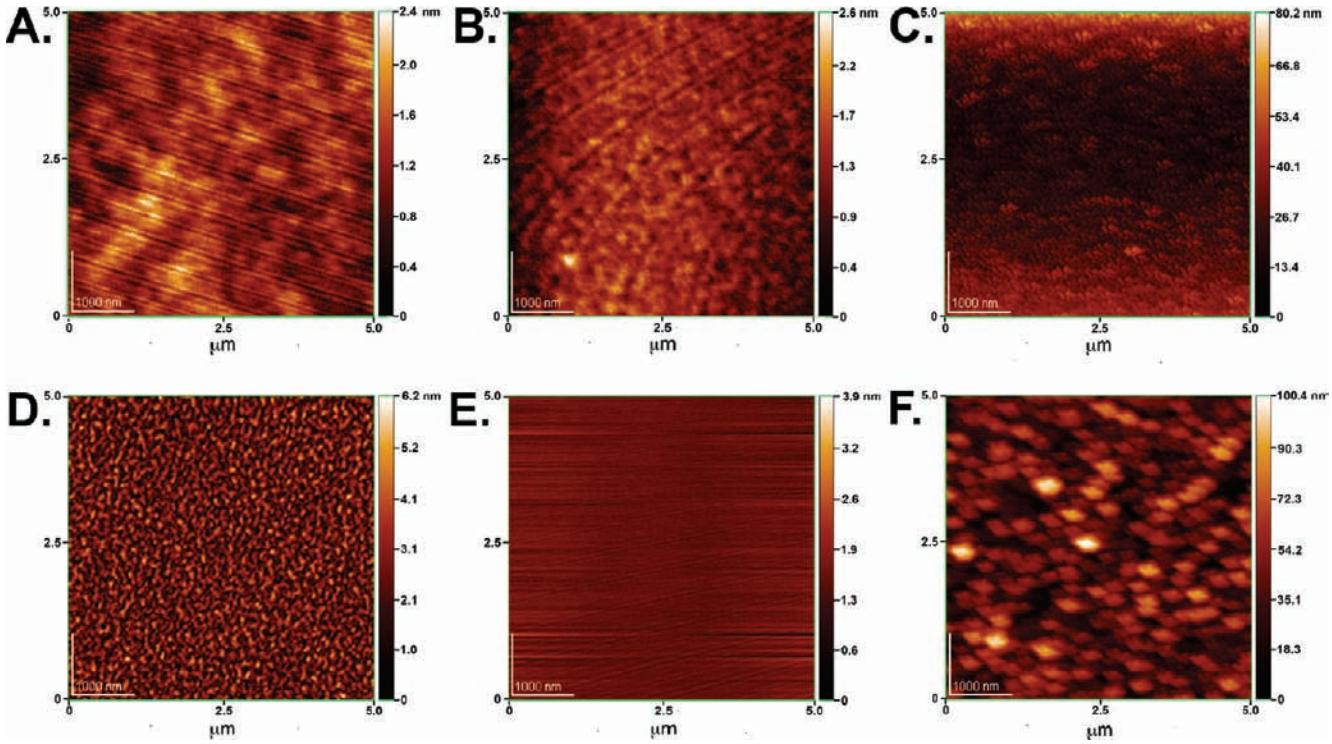

Figure 7. Contact-mode AFM images of 100 nm thick films of the indicated vapor-deposited chromophores using 5 × 5 μm^2 scan areas on single-crystal silicon substrates. (A) **2a** (rms roughness = 0.299 nm). (B) **2d** (rms roughness = 0.311 nm). (C) **2f** (rms roughness = 4.32 nm). (D) **2c** (rms roughness = 0.896 nm). (E) **2e** (rms roughness = 0.141 nm). (F) **2g** (rms roughness = 15.4 nm).

To examine Brønsted acid/base characteristics and stabilization energies involved in the various chromophore hydrogen-bonded pairs, four specific acid−base scenarios were analyzed and compared to the baseline *BzCOOH*···Py combination in **1a** (Table 3, scenario B) using Model 1 of Scheme 3. The different interactions examined include: O−H···N, C−H···O, and C−H···F. It can be seen that decreasing the hydrogen-bond donor pK_a by replacing *BzCOOH* with *BzSO$_3$H* (Table 3, scenario **B**→**A**), increases the hydrogen-bond stabilization energy (E_{sta}) by ∼6 kcal/mol. To further enhance volatility and transparency without decreasing E_{sta}, *FPOH* was substituted for *BzCOOH* in Table 3, scenario **C**. Typically, phenols have pK_a's of ∼10, but fluorine incorporation substantially increases the acidity, to pK_a ≈ 4.2 for *FPOH* and *BzCOOH*.[32,33] Computed E_{sta} values with pyridine for *FPOH* and *BzCOOH* differ by only 3%, with *FPOH* potentially providing volatility and stability enhancement. Transitioning from hydrogen-bond donor to hydrogen-bond acceptor effects, the benchmark chosen for evaluation was perfluoropyridine (*FPy*) due to its strongly electronegative character (better NLO accepting capability) and fluorine content (for volatility). Substitution of *FPy* for *Py* (Table 3, scenario **B**→**D**) decreases the E_{sta} by ∼30%, suggesting this combination is less effective in hydrogen-bonding. To further investigate fluorination effects, scenario **E** was chosen. Here out-of-plane twisting of the FPy group results from F···F nonbonded repulsion, and scenario **E** exhibits substantial diminution in E_{sta} vs scenario **B** with ∼60% decrease E_{sta}. This general decline in E_{sta} from scenario **A**→**E** correlates with computed O−H···N hydrogen-bond distance lengthening and is in agreement with reported crystal structures.[13,33] These calculated distances for scenarios **A**−**C** reveal formation of pairwise conventional hydrogen-bonds along with additional weak F···H−C or O···H−C secondary interactions.[33b] The present computed hydrogen-donor interactions (O−H···N) fall between 1.65 and 1.81 Å for **A**−**E**, in agreement with experimental crystal structure data (1.658−1.98 Å). The computed secondary interaction distances (e.g., for F···H−C and O···H−C) also fall within experimental ranges.[33c]

To further investigate the impact of interchanging hydrogen-bond donor and acceptors in Table 3, scenarios **A**−**E**, we next investigated how these very same pairs, via hydrogen-bonding, influence computed chromophore optical absorption (λ_{max}) and β response using Scheme 3, scenario **2a** as the computational template. Typical calculations involved chromophores **1a** and **2a**−**h** and required using Model 2a so to compute the extrinsic hydrogen-bond dependent response. Note that computations using Model 2a and 2b in Scheme 3 give nearly identical hyperpolarizabilities, so for simplification and computational efficiency, Model 2a was implemented in all studies. Computed complex (Model 2a) and uncomplexed chromophore λ_{max} and β properties are summarized in Tables 1 and 2, respectively. For all monomeric structures, $\Delta\lambda_{max}$ is found to be positive with the exception of **2f** and **2g** derived from **1a**. Of the bathochromically shifted chromophores, **2e** exhibits the greatest displacement ($\Delta\lambda_{\mathbf{2e}}{}^{+}$ = 86 nm). As for the hydrogen-bonded chromophores (Model 2a), those possessing twisted phenyl-benzoic acid (*PhBzCOOH*) (**2c**) and twisted phenyl-tetrafluorophenol (*PhFPOH*) (**2g**) units exhibit negative $\Delta\lambda$ values versus monomer **1a**, where substitution of *BzSOOOH* for *BzCOOH*, to give **2a**, affords the largest $\Delta\lambda$ = +178 nm. In general,

(32) (a) Castro, E. A.; Angel, M.; Arellano, D.; Santos, J. G. *J. Org. Chem.* **2001**, *66*, 6571. (b) Samuels, J. A.; Folting, K.; Huffman, J. C.; Caulton, K. G. *Chem. Mater.* **1995**, *7*, 929.

(33) (a) Kutt, A.; Leito, I.; Kaljurand, I.; Soovali, L.; Vlasov, V. M.; Yagupolskii, L. M.; Koppel, I. A. *J. Org. Chem.* **2006**, *71*, 2829. (b) Arora, K. K.; PrakashaReddy, J.; Pedireddi, V. R. *Tetrahedron* **2005**, *61*, 10793. (c) Bowers, J. R.; Hopkins, G. W.; Yap, G. P. A.; Wheeler, K. A. *Cryst. Growth Des.* **2002**, *5*, 727. (d) Schultz, T. W. *Ecotoxicol. Environ. Saf.* **1987**, *14*, 178.

Table 3. DFT-Minimized Hydrogen-Bonding Scenarios **A**−**E** with Computed Hydrogen-Bond Distances (O−H···N, C=O···H, C−F···H) and Stabilization Energies (E_{Sta})

Scenario	H-Bond Type	Distance (Å)	E_{Sta} (kcal/mol)[a]
A. 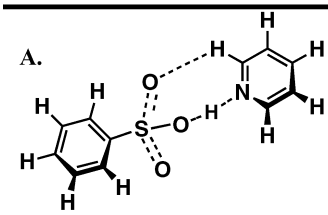	N-H	1.65	-19.4
	O-H	2.52	
B. 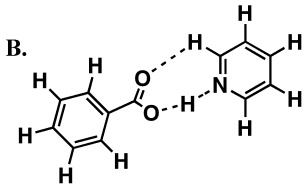	N-H	1.74	-13.6
	O-H	2.317	
C. 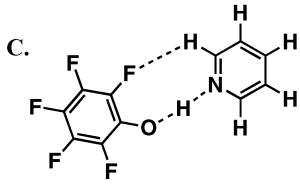	N-H	1.76	-13.2
	F-H	2.318	
D. 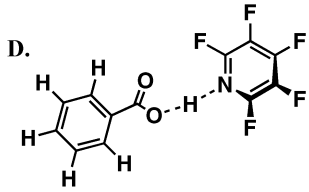	N-H	1.77	-9.69
E. 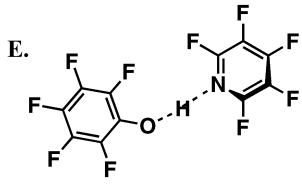	N-H	1.81	-5.60

[a] $E_{sta} = E_{complex} - (E_D + E_A)$, where E_D is the computed hydrogen-bond donor fragment energy (benzoic acid, benzene sulfonic acid, or perfluorophenol) energy and E_A is the computed hydrogen-bonding acceptor energy (pyridine or perfluoropyridine) energy, and Ecomplex is the computed complexation energy.

BzCOOH-containing chromophores, with the exception of **1a** and **2b**, exhibit a negative $\Delta\lambda$ response, whereas the optical absorption maxima in *FPOH* systems **2f**−**2h** are red-shifted. Conjugative decoupling via a methylene or twisted biaryl groups results in completely opposite optical maximum shifts of $\Delta\lambda = +8$ nm and $\Delta\lambda = -12$ nm for hydrogen-bonded methylene structure **2b** and twisted biaryl chromophore **2c**, respectively. Note that chromophores **2c** and **2d** exhibit similar $\Delta\lambda_{max}$ values, resulting from *FPy* and twisted biaryl components, and exhibiting $\Delta\lambda = -12$ and -9 nm, respectively, with both modifications being essentially additive as seen in the **2e** data (Table 1). *FPOH* and *BzCOOH* conjugative decoupling also promotes hypsochromic shifts in λ versus the hydrogen-bond versions of **2f** and **1a** ($\Delta\lambda_{\mathbf{1a}\rightarrow\mathbf{2c}^-} = -18$ vs $\Delta\lambda_{\mathbf{2f}\rightarrow\mathbf{2g}^-} = -19$ nm). Regarding combined biaryl decoupling and *FPy* incorporation in phenolic chromophore systems, a bathochromic shift of 5 nm is observed in the **2f**→**2h** transition, rather than the hypsochromic shift observed for **1a**→**2e**. Lastly, using Model 2a, the **1a**→**2a** transition affords the greatest $\Delta\lambda$ when the Brønsted acidity is increased using *BzSO₃H*.

Using the states derived from the INDO/S computations, hyperpolarizabilities (β) were next computed for each chromophore molecule. The results (Table 2) follow trends similar to those of λ_{max} where π-system decouplings (**2b**, **2c**, **2e**, **2g** and **2h**) and *FPy* introduction (**2d**, **2e**, and **2h**) afford larger β responses. In the absence of hydrogen-bonding, structure **2e** ($\beta_{calc}(\omega = 0.0) = 238 \times 10^{-30}$ esu) is found to exhibit the greatest response (Table 2). However, conjugative decoupling via twisted biaryl groups alone yields minimal increases in β for the *BzCOOH*-containing systems. Furthermore, chromophores having an *FPOH* substituent as the hydrogen-bond donor do not exhibit similar effects due in part to the lack of a secondary-amine as in **1a** (e.g., **2f** vs **1a**). This secondary amine removal significantly alters how the molecules respond to donor−acceptor location since without the secondary amine, π-conjugation is extended to the electronegative perfluorophenol

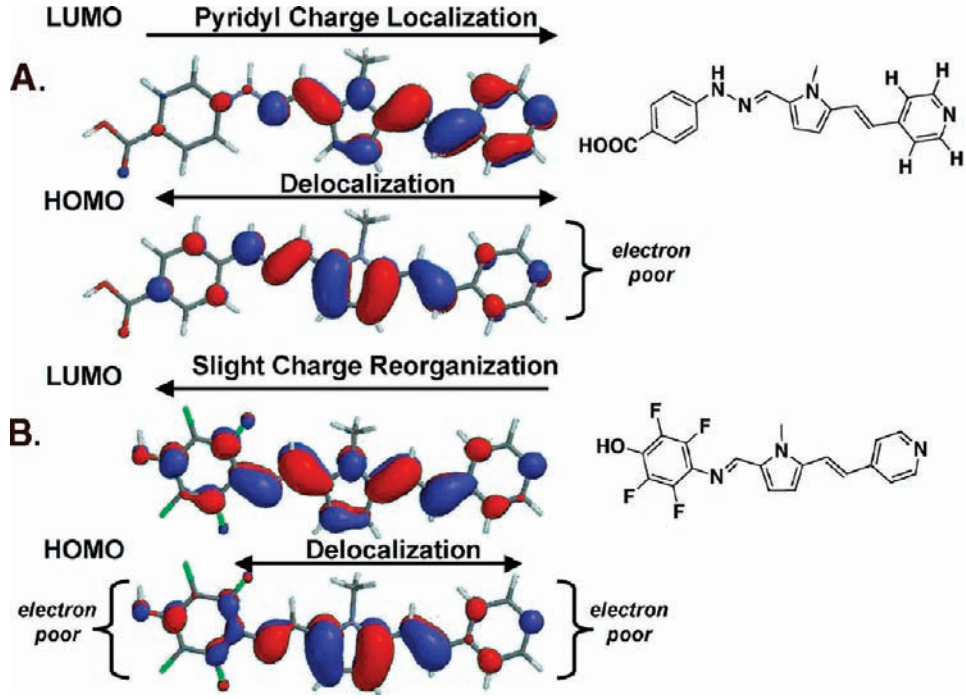

Figure 8. Computed HOMO and LUMO electron density contours of chromophores **1a** (A) and **2f** (B). (A) Electron delocalization for a donor-π-acceptor-type chromophore where density accumulates in the electron-deficient pyridine in the LUMO. (B) As a result of near-complete backbone conjugation, electron density is slightly more localized on the competing perfluorophenol fragment versus the pyridine.

ring, allowing competition for charge (Figure 8). Upon the introduction of a backbone biaryl fragment (chromophore **2f**→**2g**), the reduction in β and dipole moment suggests that *FPOH* acts as an acceptor and that the biaryl twist is effective in decoupling the hydrogen-donor source, which is more electronegative (Tables 2 and 3).

To simulate bulk response changes in vapor-deposited films, Model 2a structures were next implemented in computing hyperpolarizability changes resulting from film growth, for each molecule independently. In comparison to monomeric chromophore **1a,** the computed β response of chromophores **1a** and **2a**−**h** reveals increases in the range 3.5 − 1,370 × 10^{-30} esu with introduction of hydrogen-bonding (Table 2). The greatest increase is for chromophore **2a** with $\Delta\beta$ = 1,370 × 10^{-30} esu (~4000%). We suggest that increased pyridyl charge development (Figure 9A) leads to enhancement in dipole moment (μ) and to a decrease in HOMO−LUMO gap (e.g., Table 4, **2a**, monomer → complex), effectively increasing β according to the classical two-level model. As is the case of **2a**, the greater acidity/stabilization energy versus carboxylic acid chromophores such as **1a** leads to greater pyridyl-localized charge, and thus to greater charge separation.

The other acidic motif studied was the *FPOH* group which was incorporated to provide greater optical transparency regarding C−H overtones[1,17] as well as greater volatility. Due in part to the aforementioned intramolecular electron-accepting capacity, electronegative *FPOH* induces a $\Delta\beta$ of 11 × 10^{-30} esu (33%) versus **1a**. Other notable β increases versus chromophore **1a** are seen in structures **2b** and **2c** where $\Delta\beta$ = 79.3 (~400%) and 14.1 × 10^{-30} esu (30%), respectively, which evidence pronounced conjugative decoupling. Regarding *FPy*-containing chromophores **2d**, **2e** and **2h**, hydrogen-bonding is seen to have an opposite effect on β versus **1a**, decreasing the overall response. The largest β decrease, using structural Model 2a, is observed for **2e** where $\Delta\beta$ = −97.0 × 10^{-30} esu (41%). Overall, comparing all the hydrogen-bonded chromophore systems to **1a**, significant computed hydrogen-bonding β enhancements appear possible, without major alternations in molecular structure.

To further probe hydrogen-bond influence on multimolecular assemblies, the head-to-tail dimers and trimers depicted in Models 2−4 of Scheme 3 were analyzed. Here the motivation is that the constituent molecules, when properly assembled, dictate bulk EO properties. Because molecular π-electron properties are sensitive to delocalization changes which induce corresponding changes in transition dipoles and optical excitation energies, adjacent and/or interacting molecules may also affect optical properties, hence bulk NLO response.[17] For simplicity, we neglected cofacial $\pi-\pi$ stacking interactions because of their relative weakness compared to the head-to-tail hydrogen-bonding energies, with the exception of **2a** (see below). To examine additivity effects in each multimolecular structure (e.g., Figures 10A, B, C, D, and E), we treated each molecule within a cluster as if subjected to the same hydrogen-bonding interactions by using a hydrogen-bond donor as in Model 2a at the terminus of each cluster (Figure 10). All other things being equal, if a chromophore aggregate grows as a linear chain, the individual aligned β components should theoretically sum so that the macroscopic response ($\chi^{(2)}_{zzz}$) remains constant.[17e,h] To achieve a net effective β enhancement, the component molecular dipole moments should be aligned in a head-to-tail orientation with β increasing with hydrogen-bond strength.[17e,h] However, even with hydrogen-bonding directed acentric growth, optimal responses may not be observed due to competing forces (e.g., Figure 10, Scenarios **A**−**C**). Depending on the hydrogen-bonding moieties, computed molecular clusters may pack in a "zig-zag" fashion (Scheme 4, Table 5), regardless of the tilt angles observed in films.[7−11] This packing mode reduces response additivity by not taking full advantage of the response parallel to the molecular long axes (β_{vec}). The present modeling

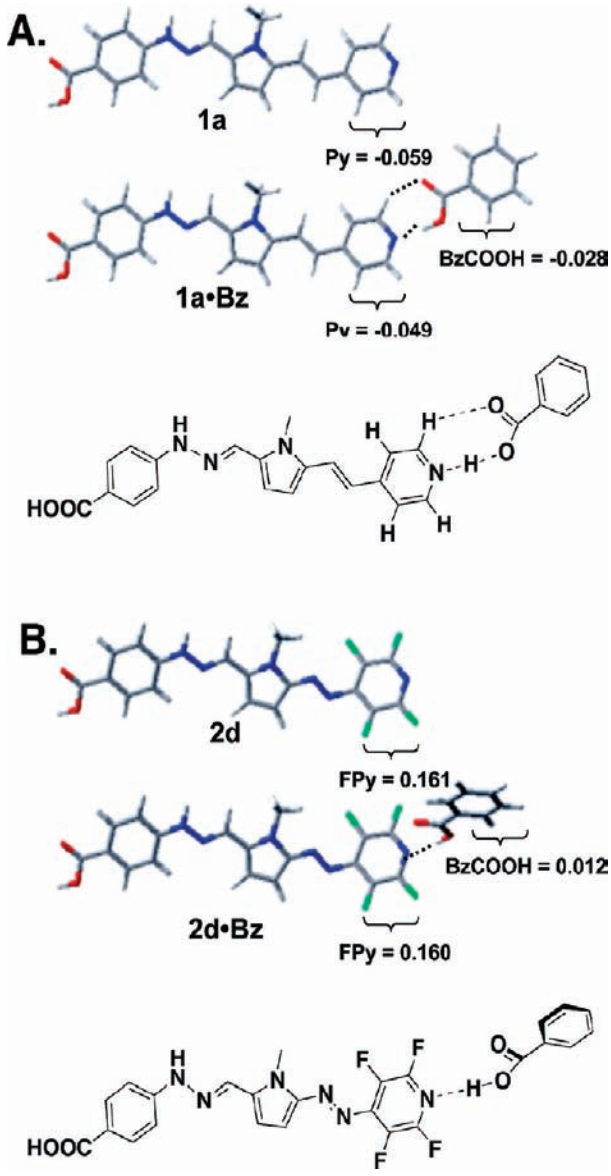

Figure 9. Mulliken charge population analysis for chromophores **1a** (A) and **2d** (B). Charges for *Py*, *FPy*, and *BCOOH* represent the total computed charge for the constituent atoms composing these fragments. (A) Upon complexation of **1a** with benzoic acid, there is concomitant charge reduction at *Py* with charge redistribted to the hydrogen-bonding *BzCOOH*. (B) Complexation of **2d** with benzoic acid evidences the opposite effect where the electron-deficient perfluoropyridine ring becomes slightly more electron-rich upon hydrogen-bonding.

approach accounts for this effect. However, when using Model 2a (monomer + donor), a correction must be applied to obtain the actual response, β_a (defined in the Theoretical section). It is $3\beta_a = \beta_{trimer}^{total}$, which is the total response obtained using the procedures given in the text and in Table 5, with geometries from Figure 10. Computed dipole moment changes ($\Delta\mu$) and hyperpolarizabilities of the monomer, head-to-tail dimer, and head-to-tail trimer of each chromophore are summarized (Tables 4 and 5).

The EO responses of chromophores **1a**, **2c**, and **2d** evolve linearly on catenation as judged by the additivity of both their corresponding hyperpolarizabilities and dipole moments. For example, **2c** which minimizes in a computed linear helical fashion due to the twisted molecular geometry (Figure 10B), not only exhibits increased response on complexation (Table 3), but the β response of trimer **2c···2c···2c** is also approximately 3× greater than that of Model 2a for chromophore **2c** (Table 5), despite the helicity. The helical growth motif derives from the biphenyl twist which propagates through successive *BzCOOH*···Py interactions among chromophore **2c** units (Figure 10), while increasing the interaction angle (θ_d) between two adjacent head-to-tail units by 2°.[11] Further modification of **1a** by exchange of *FPy* for *Py* (chromophore **1a→2d**) lead to a decrease in the linearity-defining angle θ_d between the molecular long axes (Figure 10C, **2d**) by 14° versus that of **1a**. Also, unlike **2c**, which exhibits minimal loss in response additivity due to geometrical alignment, **2d**, with a large intramolecular β, undergoes slight reduction in the calculated response and dipole moment due to the zigzag like growth pattern (Figure 10D, B versus D). From the computationally generated **2d** arrays, there is only a minor decline in monomeric chromophore μ and β properties of ~6% versus molecular arrays with axes aligned linearly (Table 5). As a result, these intermolecular interactions specific to **2d** play a much smaller role in **1a** (θ_d = 173°) and **2c** (θ_d = 175°) aggregates where the changes in μ and β are only ~1% and ~0.3%, respectively. Nevertheless, chromophore **2d**, in part due to the large intramolecular β response (as discussed above), still exhibits the greatest overall response additivity and maintains a linear growth mode as evidenced both by experimental SHG data and modeling.

For sake of completeness, the *FPOH*···Py interaction was also analyzed for chromophore **2f**. Here, when compared to **1a**, the angle between adjacent molecular long axes decreases by ~25%, impacting the dipole moment and β response additivity. In the progression, **2f → 2f···2f···2f**, there is a ~20 and 25% reduction in total μ and β, respectively due to θ_d. This first example here of a computationally -generated cluster in which the hydrogen-bond donor directs nonlinear growth, is in agreement with the experimental SHG spectroscopic results which evidence a large $\chi^{(2)}_{zzz}$ reduction with increasing film thickness (Figure 5B). Further addition of a biaryl subunit (**2f→2g**) and the substitution of *FPy* for *Py* (**2g→2 h)** affords chromophores **2g** and **2h**. Using Models 2−4, clusters of **2g** and **2h** (not shown) also exhibit nonlinear growth characteristics, much the same as **2f** in Figure 8D. From the computational and experimental results, it is evident that the *PFOH* group does not efficiently direct acentric growth.

The final pairing motif analyzed was that of **2a** (*BzSO$_3$H*···Bz). Substitution of *BzSO$_3$H* for *BzCOOH* affords the largest β while evidencing nonlinear aggregating effects. The dimer stabilization energy ($E_{sta}(\pi-\pi)$) is found to be the

Table 4. Calculated Changes in Dipole Moment ($\Delta\mu$) and HOMO−LUMO Energy Gaps for Monomers and Model 2a Structures (Donor-H···Chromophore) for Chromophores **1a** and **2a**−**h**

	monomer		complex (Model 2a)	
chromophore	$\Delta\mu$ (debye)[a]	ΔE_{gap} (eV)[a]	$\Delta\mu$ (debye)[a]	ΔE_{gap} (eV)[a]
1a	1.05	6.10	2.68	6.08
2a	1.39	6.07	37.31	1.53
2b	0.197	6.33	6.80	6.02
2c	0.079	6.12	3.97	6.02
2d	6.58	5.50	7.35	5.53
2e	7.86	5.40	7.13	5.46
2f	3.98	6.06	4.65	6.03
2g	0.046	6.28	2.75	6.20
2h	6.64	5.74	5.71	5.74

[a] Data come from geometry optimization (DFT) followed by INDO/S semiempirical analysis.

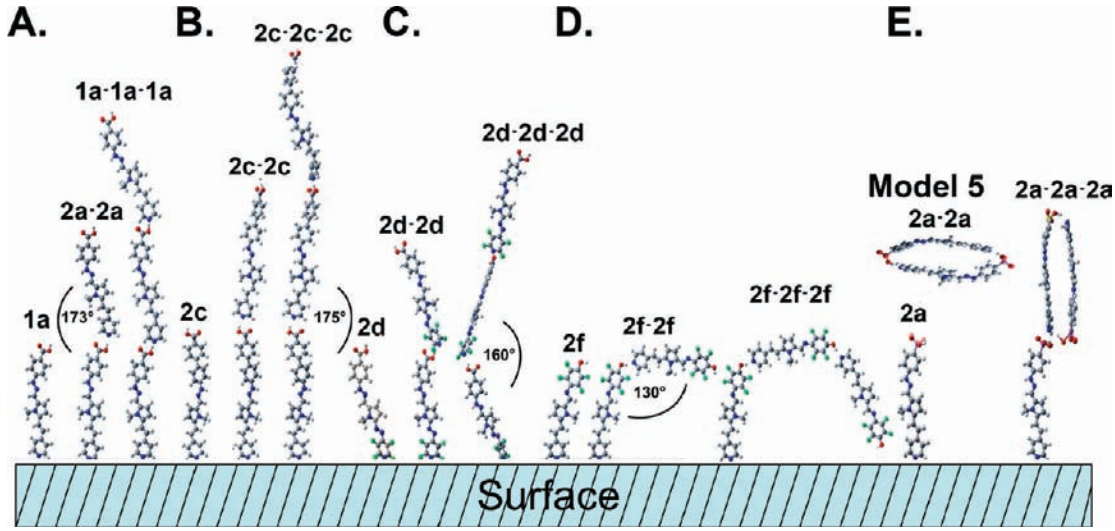

Figure 10. DFT monomeric and cluster optimized geometries of chromophores **1a**, **2a**, **2c**, **2d**, and **2f** along with the computed angles formed (θ_d) between the molecular long axes of two adjacent head-to-tail molecules specified in Scheme 4. The simulated surface represents a series of different hydrogen-bonding donors specific to each chromopohore (e.g., chromophore **1a** would use *BzCOOH* as the donor and chromophore **2f** would use *PFOH* as the donor). Hydrogen-bonding motif cluster combinations: (A) *BzCOOH*·Py, $\theta_d = 173°$, (B) *BBzCOOH*·Py, $\theta_d = 175°$, (C) *BzCOOH*·FPy, $\theta_d = 160°$, (D) *FPOH*·Py, $\theta_d = 130°$, (E) *BzSO₃H*·Py.

Table 5. DFT Optimized Structures of Chromophores **1a**, **2a, 2c**, **2d,** and **2f** using Models 2a, 3, 4, and 5 of Scheme 3[a]

structure	μ (Debye)	$\beta_{tot}(\lambda = 0.0$ eV), $\times 10^{-30}$ esu
1a	2.82 (2.85)[b]	25.6 (25.3)[b]
1a·1a	5.69	52.5
1a·1a·1a	8.50	77.3
2a	72.6	1390 (1407)
2a·2a	7.02	6.83
2a·2a·2a	80.2	1705
2c	3.37 (3.38)	37.1 (37.2)
2c·2c	6.77	74.8
2c·2c·2c	10.22	111.4
2d	4.63 (4.93)	144 (153)
2d·2d	9.31	292
2d·2d·2d	13.93	439
2f	3.17 (4.14)	57.9 (75.6)
2f·2f	5.98	85.1
2f·2f·2f	2.54	33.2

[a] Structural data correspond to the optimized geometries in Figure 8A−E. Dipole moment and hyperpolarizabilities changes are calculated using the methods described in the text. [b] Values in parentheses represent calculated dipole moment and β responses without adjustment (μ_l and β_l) using Scheme 4. The remaining values are obtained from INDO/S and SOS output files. SOS accounts for the zigzag tendencies since it is calculating the β_{zzz} along the cluster backbones.

greatest of all $\pi-\pi$ stacked systems using Model 5 of Scheme 3. Comparison of **1a** and **2f**, each with $E_{sta}(\pi-\pi) = -3.2$ and -4.4 kcal/mol, respectively, to the energy of **2a**, $E_{sta}^{\pi-\pi} = -22.3$ kcal/mol, along with the head-to-tail $E_{sta}^{H-bond} = -25.3$ kcal/mol, gives an indication of the potential for aggregation in either orientation. As for trimeric complex **2a···2a···2a**, addition of a third unit yields a unique computed structure in which the first two molecules are aligned head-to-tail with the third preferring antiparallel alignment (Figure 10E). This DFT-minimized structure exhibits a β only 315×10^{-30} esu greater than that of the monomer, 1390×10^{-30} esu, due to the centrosymmetric molecular arrangement (Table 5). The latter two growth patterns (Figure 10D and E) emphasize the importance of $\pi-\pi$ stacking, the negative effect it can have on acentric microstructure evolution, and that it cannot be overlooked in modeling high-response hydrogen-bonded molecules EO materials design.

Discussion

Chromophore Response and Hydrogen-Bonding Scenario. The consequences of five distinctive hydrogen-bonding chromophore scenarios (**A**−**E**, Table 3) were studied with the goal of optimizing response in monomeric (β) and bulk hydrogen-bonded ($\chi^{(2)}$) forms, while optimizing monomer volatility/thermal stability for vapor-phase (PVD) film growth processes. Using the benchmark *BzCOOH*···Py combination **1a**,[11a] we are able to systematically alter structure and gain insight into manipulating the aforementioned molecular properties. Fluorine-rich building blocks were chosen because of their well-known ability to enhance volatility[17] while offering increased NIR transparency at telecommunication wavelengths (1.33 and 1.55 μm). In addition, a strongly Brønsted acidic sulfonic substituent was chosen to investigate the affects of maximizing hydrogen-bond strength.[13e] Without making excessive molecular structure modifications, perfluoropyridine (*FPy*), perfluorophenol (*FPOH*), and benzene sulfonic acid (*BzSO₃H*) chromophore components were chosen. We find that, with proper structural combinations, sublimation temperatures can be lowered by ~40 °C via introduction of these substituents into the benchmark **1a** skeleton (Figure 1), while achieving sufficiently stable hydrogen-bonding to amplify EO response and direct acentric film growth. The greatest intrinsic enhancements in volatility and β are achieved using *FPy*, which increases the electron-accepting properties over **1a** while demonstrating comparable hydrogen-bonding strength in combination with *BzCOOH* groups (*BzCOOH*···FPy, chromophores **2d** and **2e**; Tables 1 and 2). Calculated and experimental optical absorption maxima also experience red shifts typical of planar high β chromophores. To further understand these substituent effects, we also examined how λ_{max} and β change with the onset of hydrogen-bonding. Note, in efforts to examine these relationships experimentally, due to solubility limitations and likely DMSO hydrogen-bonding with the present substituent combinations (with the exception of *BzSO₃H*···Py), standard measurement techniques such as

EFISH and HRS are uninformative in quantifying hydrogen-bond-dependent molecular response. Furthermore, bulk response measurements on these materials such as SHG, cannot quantify multichromophore architecture response absent hydrogen-bonding.[23] Therefore, computation and optical spectroscopy are arguably the most useful tools here.

It is found that the onset of hydrogen-bonding in *BzCOOH*-containing chromophores, in particular *FPy*-based systems, depresses the computed β response by up to 97.0×10^{-30} esu (41%) in Model 2a. Comparison of changes in Mulliken charge distribution and HOMO−LUMO energy gap, for **1a→Py···1a** (complexed, Model 2a) and **2d→Py···2d**, support this finding (Table 4, Figure 9A, B). Here, decreased energy gap and increased pyridyl electron-deficiency (q becomes more positive by 0.01) accompanying hydrogen-bonding in **1a** is not evident in **2d** (Table 4). Instead there is an increase of 0.03 eV in the HOMO−LUMO gap, along with a concomitant increase in charge q of ~0.001 on the pyridine ring as depicted in Figure 9.[34] This unexpected change in chromophore **2d** is further supported by the film data on **2d** and **2e,** which exhibit bathochromic shifts in λ_{max} versus DMSO solutions. One reason for this subtle difference in *BzCOOH*···Py vs *BzCOOH*···FPy hydrogen-bonding may involve out-of-plane interactions observed in the computed **2d** dimer and trimer clusters (Figure 10). As noted above, *BzCOOH*···Py is typically a pairwise coplanar interaction,[33b] while *BzCOOH*···FPy, in Figure 9B and Table 3 scenario D, exhibits repulsive interactions between the electron-poor perfluoropyridine ring and the carbonyl of the adjacent benzoic acid (Figure 9B). This twisting is a plausible reason for the increased perfluoropyridine charge in the Mulliken analysis, and for the intrinsic β reduction in all *FPy*-containing benzoic acid chromophores.

Regarding the hydrogen-bond donor, fluorine incorporation was explored in *FPOH* (**2f**−**h**). Since hydrogen-bonding serves two purposes, chromophore alignment and response tuning, the motivation was to introduce a hydrogen-bond donor having a pK_a similar to benzoic acid, but with greater hydrogen-bond stability.[13d,17,33d] At the most basic level (Model 1), computation predicts an E_{sta} similar to *BzCOOH*···Py (Table 3), supported by the experimental p$K_a \approx 4.10$.[33a] In further substituting *FPOH* for *BzCOOH* to give chromophore **2f**, note that fluorine effects minimal increases in volatility (Figure 1) where both **2f** and **2g** exhibit sublimation temperatures similar to **1a**, while **2g** with a greater molecular weight, sublimes at a slightly higher temperature. While introducing *FPy* reduces the sublimation temperatures of **2d** and **2e**, the greatest effect versus **1a** is evident in highly fluorinated **2h**, ~50 °C. Since *FPOH* introduction has a relatively small impact on volatility, while *FPy* enhances volatility, and since their combinations with each other and with *BzCOOH* slightly increase volatility, the question arises as to whether the volatility enhancements are due solely to fluorination or to sterically induced oxygen−fluorine hydrogen-bonding disruption. Comparison of the TGA data (Figure 1) with computed E_{sta} trends (Table 3) for the various substituent combinations reveals a direct relationship between E_{sta} and volatility, where in proceeding from scenarios B→E, chromophore sublimation temperatures fall in the order: **1a** > **2f** > **2d** > **2h**, with a parallel decrease in E_{sta} of ~60%, corresponding well with intermolecular interaction changes dependent on fluorine location.[11a] Here, scenario C versus B (Table 3) evidences a slightly weaker donor capacity, evident in the slight drop in E_{sta}, while the C→D transition evidences destabilization due to nonbonded O···F repulsion as opposed to pairwise hydrogen-bonding. The last scenario, E, fits chromophore **2h**, where F···F repulsion and lower acidity further weaken hydrogen-bonding, thus affording greater volatility.

Another important structural modification introduced in *PFOH* chromophores **2f**−**h**, is deletion of the secondary-amine fragment to assess *PFOH* electron-withdrawing properties. This group serves as an electron-rich substituent in chromophores **1a** and **2a**−**e** for charge transfer to the electron-poor pyridine rings. Amine deletion allows greater π-communication along the chromophore backbone, as noted above. We observe that *FPOH*-bearing chromophores, with the exception of **2h**, have blue-shifted absorption maxima vs **1a** in DMSO solution, thin films, and in INDO/S computed transitions (Table 1).[11a] These spectroscopic patterns, along with a larger computed HOMO−LUMO gap (Table 4) at first suggest potential β response reduction due to the amino group deletion, however the increase in dipole moment by ~3× and ~30% increase in computed β response argue otherwise (Tables 1 and 2). From both the response and $\Delta\mu$ it appears that removal of the amino group causes the perfluorophenol group, as in **2f**, to act as an electron-acceptor. In agreement with monomer studies, the hydrogen-bonded thin films of **2f** exhibit red shifts in λ_{max} (both computed and experimental) along with an EO response enhancement typical of the hydrogen-bonding effects seen in **1a** (Table 1 and 2).[11a] The major difference between **1a** and chromophore **2f** is the larger EO response afforded by *PFOH*, deduced using both Model 2a and in thin film experiments of ~3× and ~30%, respectively. In terms of the classical two-level model, since both chromophores have similar calculated HOMO−LUMO gaps, the greater computed $\Delta\mu$ explains the larger response of **2f** (Table 4). Furthermore, note in the HOMO−LUMO contours of **2f** and **1a**, there is greater charge localization around the hydrogen-donor *PFOH* of the **2f** LUMO (Figure 8).

Besides manipulating response/volatility trade-offs via fluorine incorporation, EO response tuning via hydrogen-donor acidity enhancement, was of great interest. Since *BzSO$_3$H* is a stronger Brønsted acid than *BzCOOH*,[33a] chromophore **2a** was synthesized to generate greater pyridyl positive charge. Solubility properties and TGA data support increased hydrogen-bonding, with **2a** exhibiting diminished DMSO solubility and volatility (Figure 1). These solubility and volatility trends are in agreement with computed E_{sta} values (Table 3) which depict *BzSO$_3$H*···Py as a very stable hydrogen-bonding pair. In terms of computed linear optical and EO response, monomeric **2a** closely resembles **1a** (Table 1). However, including Model 2a hydrogen-bonding and thin film packing, yields the largest computed $\beta = 1407 \times 10^{-30}$ esu and experimental $\chi^{(2)} = 302$ pm/V of the present series (Table 2). From the two-level model, this enhanced response reflects a ~90% increase in $\Delta\mu$ and substantially smaller ΔE_{gap} (Tables 1 and 4). These properties are a direct result of amplifying the proton donation, whereby the pyridinium zwitterionic limit is approached.

Methylene or Twisted Biaryl Conjugative Decoupling. To increase the electron-richness of the secondary-amine substituent and to determine whether *FPOH* acts as an electron acceptor, methylene (**2b**) and twisted biaryl (**2e**, **2g**, and **2h**) chromophores were investigated. Tables 1 and 2 indicate $\Delta\lambda$ shifts and nearly 4-fold increases in β due, in part, to the conjugative decoupling from the electron-withdrawing *BzCOOH* group. Studies of chromophore **2b** were restricted to computational modeling and

(34) (a) Gutman, V. *Rev. Chim. Roum.* **1977**, *22*, 679. (b) Gutman, V. *The Donor Acceptor Approach to Molecular Interactions*; Plenum: New York, 1978; p 122.

linear optical analysis because of thermal degradation on sublimation, presumably due to decarboxylation.[11c] As for the twisted biaryl with *BzCOOH* as a substituents, such chromophores exhibit good thermal stability (Figure 1). However, NLO response data argue that **2c** exhibits only a slightly larger $\chi^{(2)}_{zzz}$ than **1a**, but with a unique computed/experimental hypsochromic optical absorption shift (Table 1). As in the *FPy*-containing chromophores, this shift may reflect intermolecular cofacial packing interactions in the films, modified by the twisted biaryl.[17a,h,f] This result may account for what appears to be reduced response in **2c**, evident when comparing computed hydrogen-bonding response gains (Model 2a) to measured SHG response in **1a**. Here, a 45% difference in computed and measured response is observed. This discrepancy may reflect neglect of three-dimensional packing in the computation.

To further understand the interplay of conjugative decoupling and fluorination, and their effect on β, chromophores **2e**−**h** where studied. Commonality in computational and experimental optical data for **2d** and **2e** argue for similarities in hydrogen-bonding (Tables 1 and 3). In the absence of hydrogen-bonding and resonant enhancement, both SOS computational and experimental SHG results verify that **2e** has the largest response of this chromophore family. However, chromophore **2e** is structurally similar to **2d** and experiences the same charge donation, via the carbonyl group adjacent to *FPy*, which weakens the hydrogen-bonded β response (Table 2). For 50 nm double-sided films, chromophore **2e** exhibits a greater NLO response than **1a**, **2a**, **2c**, **2e**, **2g**, and **2h**-derived films, but still less than **2d** films, probably due to reduced resonance enhancement versus λ_{max} = 551 nm (**2d**). Introduction of biaryl-conjugative decoupling in **2f** yields chromophore **2g**, for which both SHG and computation reveal slight decreases in $\chi^{(2)}$ and β, due in part to diminished conjugation with the accepting *FPOH* unit. This decrease is accompanied by hypsochromic shifts in computed and measured λ_{max} versus **2f**, along with a reduced dipole moment and increased HOMO−LUMO separation. Unlike the aforementioned "twist-decoupled" chromophores, **2h** does not exhibit a negative $\Delta\lambda_{max}$ compared to **1a** upon hydrogen-bonding, but rather red-shifts. This increased NLO response is due again to the *FPy* substitution and the "twist." In general, introduction of *FPy* and twisted biaryl groups ensures charge transfer analogous to that in chromophore **1a**, but with enhanced EO response.

Hydrogen-Bonding Effects on Film Microstructure and Morphology. Utility in electro-optic devices imposes EO materials requirements, including noncentrosymmetric microstructure and its long-term stability.[1−3,17] Since the present hydrogen-bonding-assisted film-growth process relies on self-organization from the vapor-phase,[11] unlike SAS materials[7−10] and poled polymers,[1−3,5] it is essential that the component molecules direct linear, acentric growth as successive layers undergo nucleation.[14] Furthermore, as in zwitterions, hydrogen-bonding interactions will induce dipoles due to partial charge development.[2a,14a−c] Such dipolar interactions may favor antiparallel $\pi-\pi$ stacking self-assembly rather than head-to-tail axial growth.[2a] In terms of thermodynamics, the growth pattern will depend on the intrinsic hydrogen-bond strengths, on the geometry in which the hydrogen-bonding is arrayed, and on the charge distribution. Previously, it was demonstrated by SHG spectroscopy that chromophore **1a** undergoes linear (i.e., uniform evolution of acentricity) growth up to ∼1 μm thick films, after correction for self-absorption.[11a] In the present assessment of hydrogen-bonding moieties and their effect on film microstructure, we have implemented DFT as a predictive tool. Support for this approach (Scheme 3) comes from energy-minimized results for **1a** monomers, dimers, and trimers, which exhibit chromophore stacking regularity with μ and β additivity after correcting for head-to-tail angles (Scheme 4, Scenario A, Figure 10). For **1a**, the computed dimer head-to-tail angle (θ_d) is ∼173°. As a result of the regular film microstructure, indicated by the SHG measurements and cluster calculations, the film morphology is also very smooth.[11a] With good agreement between experiment and computed geometries (depicting β response additivity), this approach was applied to chromophores **2a**, **2c**, **2d**, and **2f**.

To gain further insight into *FPy* influence on the film growth process, we chose chromophore **2d** as a model system. Here, unlike the pairwise hydrogen-bonding of *BzCOOH*···Py in **1a** (Table 3, Motif C),[11a,32] there is a twist of ∼86° from molecular planarity, with the carbonyl group oriented toward the electron-deficient *FPy* π cloud, creating a 160° angle at the head-to-tail junction of two monomers. This interaction (see Figure 10C) decreases the effective hyperpolarizability by ∼6% (using Scheme 4) upon assembly, while still directing favorable gas-phase linear alignment. SHG analysis (Figure 5A) of **2d** film growth reveals linear increase in $(I^{2\omega})^{1/2}$ with increasing film thickness, further supporting growth Models 2−4 in Scheme 2. Also, indicative of microstructural regularity, AFM images reveal smooth films with rms roughness = 0.31 nm (Figure 7B).

To enhance the donor portion efficiency of the **1a**-based donor-π-acceptor structure, decoupling of the chromophore from the hydrogen-bond donor was accomplished by inserting either a twisted biaryl (**2c**) or methylene fragment (**2b**). Due to thermal instability, **2b** was not studied extensively. Instead, emphasis was placed on understanding twisted biaryl effects on film growth. Comparison of chromophores **2c** and **1a** reveals an increased dimer head-to-tail angle of 2° in Figure 10B, with additivity of both dipole moment and β response. In agreement with the **2c** cluster computational result, linear SHG response with film thickness correlates with regular acentric film growth (Figure 5A). An interesting aspect of the **2c** cluster result is the straightening effect that the twist induces in oligomer growth. Regarding SHG intensity near 1 μm film thicknesses, the response of **2c** films falls short of the *FPy* derivative, reflecting the intrinsically weaker accepting ability, along with diminished SHG resonant enhancement, λ_{max} = 366 nm vs 547 nm for **2d**.

Regarding *FPOH*-based chromophore systems, a different scenario is observed by DFT minimization. Here, the *FPOH* geometry along with the pairwise affinity for the pyridyl-hydrogen (C−H···F and O−H···N), severely impacts θ_d versus *BzCOOH*···Py, and may underlie the observed nonlinear chromophore film growth data (Figure 5). Structurally, the only other factor differentiating *FPOH*-based chromophores from their *BzCOOH* and *BzSO$_3$H* counterparts is the absence of the secondary-amino donor. To probe this effect, structural analysis of **2f** having an added amino group was carried out using Models 2a and 3. The computational results suggest that amino group incorporation in **2f** adjusts θ_d from 130 to 138°, significantly different from the angles observed for **1a**. Thus, θ_d depends strongly on the hydrogen-bonding interaction, as illustrated by the poor growth-directing capability of *FPOH* noted above. Similarly, chromophores **2g** and **2h** (not depicted in Figure 10) have computed gas-phase angles of 131 and 141°, respectively, predicting poor growth characteristics with "twist" and *FPy* inclusion. These modeling results favorably support the $(I^{2\omega})^{1/2}$ versus film thickness data for chromophores **2f**−**2h**, with SHG intensity saturating near 100 nm (Figure 5B). Note that the

macroscopic responses for **2f**−**2h** fall with increasing film thickness in the range ∼3−100 nm (Table 2). This result further implicates *FPOH*···Py interactions as overall poor candidates for hydrogen-bonded NLO film growth by PVD.

Typifying the energetic competition between $\pi-\pi$ antiparallel and axial head-to-tail dimerization, **2a** provides the first example of hydrogen-bond directed antiparallel alignment (Figure 10E, **2a**···**2a**···**2a**). Evidence for this is the disagreement between computation and experiment in comparing monomer to Model 2a, and DMSO to thin film optical data, where a λ_{max} blue shift of 81 nm is observed. This hypsochromic shift for 100 nm films is also observed in chromophores containing *FPy* and the twisted biaryls (discussed above). For **2a**, the 100 nm thin film optical absorption suggests a significant change in the HOMO−LUMO gap, seen also in computed and experimental SHG results (Tables 1 and 2). With λ_{max} independent of film thickness[12a] and SHG data exhibiting negligible linear growth (Figure 6), temperature-dependent solution spectroscopic methods were used to assay possible aggregation. At a maximum concentration of 1.28×10^{-3} M (due to insolubility) there are three major absorption maxima in DMSO solutions of **2a** (Figure 2C and D). Upon dilution, diminution of the 531 nm peak is observed. An aggregation model is plausible and compares well with the computed λ_{max} (monomer and Model 2a), suggesting a mixture at 1.28×10^{-3} M of monomer and hydrogen-bonded aggregate (having a smaller HOMO−LUMO gap, larger response). The 531 nm absorption compares well with computed Model 2a of 566 nm. Dilution and increased temperature afford unaggregated monomer (nonhydrogen-bonded), blue-shifted with respect to the hydrogen-bonded aggregate. With optical spectroscopy indicating concentration- and temperature-dependent intermolecular interactions, SHG depicting the response reduction with film thickness (Figure 6), and calculations yielding similar stabilization energies ($E_{sta}^{H-bond} = -25.3$ vs $E_{sta}^{\pi-\pi} = -22.3$ kcal/mol, discussed above), it appears that **2a** may undergo centrosymmetric film growth. In the first few layers, **2a** most likely prefers hydrogen-bonding where molecules nucleate linearly, with hydrogen-bonding functioning to align molecules and enhance β via proton donation (as noted above; Table 5 and Figure 10E). With the onset of polarization, the molecular dipole moment increases with film growth rendering $\pi-\pi$ stacking more probable. The combination of hydrogen-bonding and $\pi-\pi$ stacking as in Figure 10, scenario E, **2a**···**2a**···**2a**, greatly enhances zwitterionic character, increasing the stabilization energy ($E_{sta}^{z-z} = -41$ kcal/mol).[2a,17,30] This stabilization would favor strongly hydrogen-bonded centrosymmetric pairs as in Figure 3A, with computed dimer distances in the typical 3−4 Å range.[35] When film thicknesses approach 100 nm, these pairs appear to dominate the microstructure, which is supported by the hypsochromic film λ_{max} shift to ∼362 nm and near-zero SHG response. Unlike the *PFOH*-containing films, tapping-mode AFM still indicates surface roughnesses similar to those in the other linear growth films, with rms roughness = 0.299 nm (Figure 7A).

Conclusions

The synthesis and physicochemical properties of eight new hydrogen-bonding "donor−acceptor" pyrrole-based NLO chromophores are reported. The chromophore design strategy is based on **1a** with the goal of enhancing macroscopic NLO response and stability by introducing fluorine (chromophores **2d**, **2e**, **2g**, and **2h**) and conjugative decoupling (chromophores **2c**, **2e**, **2g**, and **2h**) while assessing the impact of hydrogen-bonding donor−acceptor combinations (**2a**−**2h**) on NLO response and film microstructure. We focused primarily on three areas: (1) chromophore response dependence on hydrogen-bonding, (2) response dependent conjugative decoupling, and (3) hydrogen-bonding motif-related film microstructural effects. Depending on the combination of the hydrogen-bonding pairs, chromophores fall into three volatility classes with the order of decreasing volatility as follows: (*FPy* containing: **2h**, **2d**, **2e**) > (*FPOH* containing: **2f**, **2c**, **2g**) > (BzSOOOH containing: **2a**). Chromophores containing *BzCOOH* not only provide the most stable acentrically aligned films of the series, but also exhibit response magnitudes second only to chromophore **2a**. *FPy*-containing chromophores, in addition to being the most volatile, have the largest computed and measured intrinsic NLO responses when paired with *BzCOOH* (**2d** and **2e**). In the presence of hydrogen-bonding, *FPy*-containing chromophores computationally exhibit diminished bulk NLO response. These effects are minor in comparison to the response enhancement attained via *FPy* introduction. Introducing the *FPOH* group affords no advantages versus the benchmark *BzCOOH* motif of chromophore **1a** other than minimal intrinsic β response enhancement mainly due to inherent *FPOH*-based conjugative differences. Introducing conjugative decoupling at the hydrogen-bond donor end of the molecules (chromophores **2e**, **2g**, and **2h**) affords significant response (β and experimental $\chi^{(2)}$) gains in secondary-amine bearing molecules (e.g., **2e**). Fluorination at the chromophore accepting-end and increased separation between the hydrogen-bond donor and the chromophore secondary-amine electron-donor enhances both molecular hyperpolarizabilities and experimental film macroscopic responses.

Substitution of *BzCOOH* of **1a** for *BzSO$_3$H* has the single greatest impact on β and $\chi^{(2)}$ in **2a**, yielding $\Delta\beta = 1381 \times 10^{-30}$ esu and $\Delta\chi^{(2)} = 281.6$ pm/V which, to date, is the largest observed gain in hydrogen-bonded PVD-derived organic EO films. However strong hydrogen-bonds are believed to lead to near-zwitterionic behavior which inhibits acentric growth. Concentration- and temperature-dependent optical studies, SHG film intensities $(I^{2\omega})^{1/2}$, and computation together support the tendency of **2a** to strongly aggregate versus the other chromophores studied. Overall, there is good agreement between computation and experiment for the film growth characteristics of systems **1a** and **2a**−**2h**. These results provide new insights into how simple hydrogen-bonding motif substitution can drastically impact acentric film-formation characteristics, and intrinsic/extrinsic NLO response. In addition, these findings help to define the limits of PVD as a method for organic NLO film growth using simple hydrogen-bonding combinations, and suggest more complex hydrogen-bonding motifs and chromophores possessing intrinsically greater molecular hyperpolarizabilities.

Acknowledgment. We thank DARPA/ONR (SP01P7001R-A1/N00014-00-C) and the NSF-Europe program (DMR-0353831) for support of this research. We thank the Northwestern NSF MRSEC for support of characterization facilities (DMR−0520513), and Prof. J. Ketterson and Dr. B. Watkins for assistance with SHG spectroscopy.

Supporting Information Available: Synthetic details for the intermediates and chromophores **2a** through **2f** and film processing procedures. This material is available free of charge via the Internet at http://pubs.acs.org.

JA900131Y

(35) Letizia, J. A.; Facchetti, A.; Stern, C. L.; Ratner, M. A.; Marks, T. J. *J. Am. Chem. Soc.* **2005**, *127*, 13476.
(36) Sander, W.; Hubert, R.; Kraka, E.; Grafenstein, J.; Cremer, D. *Chem.−Eur. J.* **2000**, *24*, 4567.